This is a preprint, the final version is subject to change, of the American Mineralogist (MSA)
Cite as Authors (Year) Title. American Mineralogist, in press.
(DOI will not work until issue is live.) DOI: http://dx.doi.org/10.2138/am-2014-4785

Reflectance spectroscopy of plagioclase-dominated mineral mixtures: Implications for characterizing lunar anorthosites remotely

Leah C. Cheek[1] and Carlé M. Pieters[2]

[1]Department of Astronomy, University of Maryland, College Park, Maryland 20742, USA
[2]Department of Geological Sciences, Brown University, Providence, Rhode Island 02906, USA

REVISION 1

Submitted to: American Mineralogist special issue on the Lunar Highland Crust
Date: October 24, 2013
First Revision: April 25, 2014

ABSTRACT

Anorthositic rocks dominate the Moon's upper crust. As remnants of the lunar magma ocean (LMO), small variations in the mineralogy of these rocks may hold key information about the homogeneity of LMO composition and solidification processes. Orbital near-infrared (NIR) sensors are sensitive to mineralogy, but technologic advances have only recently enabled detection of the plagioclase component in crustal rocks based on absorption band centered near 1250 nm. Anorthosites occupy a unique mineralogic range that is well suited for NIR studies: the highly transparent component, plagioclase, is present in high abundances while the spectrally dominant mafic or oxide minerals are present in only minor abundance. As a result, spectra of anorthosites are more likely than many other rock types to contain visually discernable signatures from more than one mineral component, facilitating their identification and characterization in NIR data.

In support of the new NIR measurements for the Moon, we present laboratory spectral analyses of well-controlled plagioclase-dominated mineral mixtures. We focus on the spectral

Always consult and cite the final, published document. See http://www.minsocam.org or GeoscienceWorld

effects of varying mafic and oxide composition and abundance in mixtures with a common plagioclase endmember. The results demonstrate that plagioclase can be a significant contributor to reflectance spectra when strongly absorbing minerals are present in low abundance. We show that the contribution of plagioclase is more pronounced in mixtures with pyroxenes and certain spinels, but more easily masked in mixtures containing small amounts of olivine. Differences in minor mineral composition are clearly expressed in bulk spectra. Modeling of mixtures produced using a Hapke nonlinear approach accurately estimates mineral abundances in laboratory spectra to within 5 vol% for mixtures with ≥90 vol% plagioclase. Together, these results imply that not only should orbital NIR datasets be able to discern the presence of plagioclase in anorthositic crustal exposures, but also that detailed information about anorthosite mineral assemblages can be reliably accessed in reflectance spectra.

Keywords: Moon, anorthosite, near-infrared spectroscopy, minerals, plagioclase

1. INTRODUCTION

Reflectance spectroscopy is a valuable tool for investigating the mineralogy of planetary surfaces remotely (e.g., Adams and McCord, 1970; McCord et al., 1981). Most of the major rock-forming minerals found in the lunar sample collection can be distinguished by the positions of their diagnostic broad absorption bands across near-infrared (NIR) wavelengths (e.g., Conel and Nash 1970; Hazen et al. 1978; Burns 1993; Sunshine et al. 1998). Laboratory spectra for several of these key mineral types are shown in Figure 1. Rarely, however, do minerals occur in isolation on a planetary surface. Typically, they are mixed on a variety of spatial scales, occurring together in a range of rock types and soils. When mineral components occur in an intimate mixture, incident light interacts with multiple components before returning to the sensor and the bulk reflectance spectrum is not a simple linear combination of the endmember spectral properties (e.g., Hapke 1981). In these cases, absorbing minerals such as pyroxenes dominate spectra disproportionally to their abundance. Detailed laboratory and modeling studies are therefore required to accurately characterize the spectra of materials consisting of more than one component. These types of studies are crucial for enabling mineralogic analyses from remote spectroscopy data for the Moon and other planetary bodies.

This study focuses on the spectral characteristics of plagioclase-rich mineral mixtures relevant to anorthositic lithologies. Anorthosites contain ≥90% plagioclase (Stöffler et al. 1980) and are believed to have formed the upper crust of the Moon by accumulation of buoyant plagioclase crystals at the top of a solidifying magma ocean early in lunar history (e.g., Smith et al. 1970; Wood et al. 1970; Herbert et al. 1977; Warren and Wasson 1980; Elkins-Tanton et al. 2011; Suckale et al. 2012). Although pure plagioclase exhibits a diagnostic absorption near 1250 nm (Conel and Nash 1970), it is highly transparent and difficult to distinguish in rocks and soils when more strongly absorbing minerals are present (e.g., Nash and Conel 1974; Singer 1981; Johnson et al. 1983; Crown and Pieters 1987; Mustard and Pieters 1987; Serventi et al. 2013a). In addition, experimental studies have noted that the ~1250 nm plagioclase absorption can be erased even in the absence of strongly absorbing minerals by the transformation of plagioclase crystals into a diaplectic glass by moderate shock pressures (e.g., von Engelhardt and Stöffler 1968; Stöffler 1971). This latter process has often been invoked to explain the lack of a plagioclase absorption in remote sensing data for the Moon despite the fact that plagioclase is believed to be abundant throughout the anorthositic highlands (e.g., Adams et al. 1979; Spudis et al. 1984). Due primarily to the historic lack of identifiable plagioclase in NIR spectra for the

Moon, there has been relatively little impetus to characterize the contributions of a ~1250 nm crystalline plagioclase absorption in bulk spectra.

However, the newest generation of spectrometers orbiting the Moon have, for the first time, identified the diagnostic plagioclase absorption feature in numerous locations across the lunar surface (e.g., Ohtake et al. 2009; Donaldson Hanna et al. *in review*; Yamamoto et al. 2012). In addition, many locations also exhibit spectral properties that may indicate combinations of crystalline plagioclase and small abundances of pyroxene or olivine (e.g., Cheek and Pieters 2012). Examples of such diverse spectra are shown in Figure 2, including spectra from the Orientale basin and Copernicus and Tsiolkovskiy craters. Although the presence of mafic minerals is readily detected, the abundance and character of these components is much more difficult to determine. These specific examples are examined in detail in a subsequent section of this paper.

The goal of this laboratory study is to document the spectral characteristics of plagioclase-dominated mixtures that vary systematically in both mineral abundance and mineral composition. The approach is similar to that of Serventi et al. (2013b) who, in addition to varying mafic abundance, explore the effect of varying plagioclase composition on the spectra of plagioclase-dominated mixtures. Here, we keep the plagioclase endmember constant and document the effects of varying minor mineral chemistry and abundance on bulk spectral properties. We use pure, well-characterized endmembers in order to focus only on the fundamental systematics of plagioclase-dominated mixture spectra. This study explicitly avoids the complicating effects of space weathering and other variables in order to better isolate the effects of mineral composition and abundance. A secondary goal of this work is to use the results of the laboratory mixtures to test a nonlinear model for predicting mixture spectra from endmember spectra.

2. BACKGROUND

Broad mineral absorptions in the near-infrared are caused by electronic transitions among the d-orbitals of certain transition metal atoms, predominately iron. These transitions are brought on by asymmetries imparted to the d-orbitals by the location of the atom within a crystal structure (e.g., Burns 1993). Differences in the crystallographic sites that contain iron atoms in different rock-forming minerals result in distinguishable absorption features. Laboratory spectra of the major lunar minerals that are considered here are shown in Figure 1: plagioclase, pyroxene, olivine, and spinel. Anorthosites occupy a unique compositional range in which the highly absorbing minerals, such as pyroxenes, spinel, and to a lesser extent olivines, are present in exceedingly low abundance (≤10 vol%, nominally). By contrast, plagioclase, which is relatively transparent, is present in high abundances. As a result, anorthosite spectra are likely to display absorption features due to plagioclase *and* other minor minerals. This provides significant leverage in determining mineral composition and abundance because the composite absorptions that arise from combining overlapping minerals absorptions should be unique to a relatively restricted range of mineralogies. The effects of glass and opaque minerals such as ilmenite on bulk spectral properties are not evaluated here, although future mixing studies should explore the effects of these additional important components of lunar rocks.

Reflectance spectra of unweathered, inclusion-free plagioclase samples are characterized by a broad absorption centered near 1250 nm (e.g. Conel and Nash 1970; Bell and Mao 1973; Adams and Goullaud 1978). This absorption is caused by trace amounts of Fe^{2+} incorporated into the plagioclase structure, likely into the large 8-12 fold Ca^{2+} site. Increasing FeO content generally corresponds to increasing ~1250 nm absorption strength (Bell and Mao 1973; Serventi et al. 2013). Variations in An content (molar Ca/(Ca+Na+K) in plagioclase) correspond to small shifts (tens of nanometers) in the exact center position of the broad ~1250 nm absorption (Adams and Goullaud 1978).

Pyroxene spectra, by contrast, are characterized by strong absorptions near 1000 and 2000 nm that are due primarily to Fe^{2+} within the M2 octahedral site (e.g., Hazen et al. 1978; Cloutis and Gaffey 1991; Burns 1993). Orthopyroxenes typically display relatively short-wavelength absorption centers, near ~930 and ~1900 nm, that shift to longer wavelengths with increasing FeO content. Samples that are particularly high in iron also display a weaker band centered near 1200 nm due to Fe^{2+} partitioning onto the smaller, octahedral M1 site (e.g., Klima et al. 2007; 2011). Increasing Ca content in pyroxenes also shifts the major M2 absorptions to longer wavelengths, and spectra of high-calcium clinopyroxenes display absorptions centered near 1000 and 2200 nm (e.g., Cloutis and Gaffey 1991; Klima 2011).

Spectra of olivines display a broad, composite absorption centered near 1000 nm. This feature is comprised of a central absorption caused by Fe^{2+} transitions within the octahedral M2 site, as well as two absorptions that overlap the M2 absorption on either side caused by Fe^{2+} in the M1 octahedral site (e.g., Burns 1970; Burns 1974; Hazen et al. 1977). As olivine iron content increases, each of these three absorptions independently shifts to longer wavelengths although the M1 bands are observed to shift more strongly than the central M2 band (e.g., Burns 1970; King and Ridley 1987; Sunshine et al. 1998). At the same time, the strengths of the M1 bands relative to the M2 band increase with increasing iron abundance (Sunshine et al. 1998).

Unlike the mafic silicates, Fe^{2+} in normal Mg-spinel (an oxide) favors a tetrahedral site, resulting in strong absorptions at slightly longer wavelengths, near 2000 and 3000 nm (e.g.

Cloutis et al. 2004). For spinel with higher iron abundances, some Fe^{2+} partitions onto the octahedral site, generating weaker absorptions near 650 and 950 nm (Cloutis et al., 2004; Jackson et al. 2012; Jackson et al. submitted).

3. MINERAL ENDMEMBERS IN MIXING EXPERIMENTS

3.1 Endmember selection

The goal of this study is to characterize the spectral properties of plagioclase-dominated binary mineral mixtures that vary systematically in mineral composition and abundance. The primary objective in choosing endmembers for these mixtures was to obtain samples that are pure, homogeneous, and available in large quantities so that their compositions can be well characterized and linked to spectral properties. Because mineral composition is known to affect spectral properties in specific ways, a second goal was to select endmembers with compositions that are relevant to those observed in lunar rocks, particularly those with high proportions of plagioclase. The extent to which variations in mineral abundance, when coupled to variations in mineral composition, are expressed in spectral properties of plagioclase-dominated mixtures is the subject of the laboratory analysis described here.

The sources and compositions of specific endmembers are described in the following sections and in Tables 1 and 2. Comparisons to measured properties of lunar samples are also discussed below. We emphasize that the specific endmembers chosen are not *direct* spectral analogs for lunar minerals, which include a range of complicated optical effects due to shock metamorphism and space weathering (e.g., Adams et al. 1979; Hapke 2001). Rather, they were chosen in order to enable a systematic investigation of spectral reflectance characteristics that arise solely from variations in mineral composition and abundance, without complications from other variables. Future studies should build on the foundations provided by this simplified dataset to more closely approximate the full range of optical characteristics of lunar surface materials.

3.2 Plagioclase endmember

The plagioclase endmember used in this study is a highly pure, terrestrial gem-quality labradorite from a volcanic source in Mexico. This sample was largely chosen because of the availability of >10 grams of homogeneous, inclusion- and alteration-free material, as well as its spectral similarity to plagioclases separated from lunar highland samples (described below). A brief description of the sample is given in Table 1, and major element composition is given in Table 2. Plagioclase in lunar ferroan anorthosites is typically more calcium-rich (>An95) and slightly more iron-poor (FeO <0.3 wt%) (e.g., McGee 1993), than the terrestrial plagioclase sample used here. However, Figure 3 demonstrates that despite these subtle compositional differences, the analog sample is a good representation of the key spectral properties of lunar highland plagioclase – namely a high albedo and a prominent 1250 nm absorption. This is likely due to the fact that despite a reported influence of band center position on An number, this effect is only on the order of ~50 nm over the labradorite – anorthite compositional range (Adams and Goullaud 1978). Further, while the greater abundance of iron in the terrestrial sample may be expected to cause a relatively stronger absorption compared to lunar samples, this effect is mitigated by the fact that the *total* iron abundance in the terrestrial sample should include a substantial amount of ferric iron, which does not affect the strength of the crystal field absorption near ~1250 nm. The terrestrial sample used here is therefore an excellent analog for lunar anorthositic plagioclases, which are being identified globally by their ~1250 nm absorption bands in new orbital datasets for the Moon's crust (Yamamoto et al. 2012; Donaldson Hanna et al. in review).

Always consult and cite the final, published document. See http://www.minsocam.org or GeoscienceWorld

3.3 Other endmembers

The six non-plagioclase minerals used in binary mixtures with plagioclase for this study include two olivine samples, two pyroxene samples, and two spinel samples. Two of each mineral type were selected in order to characterize the range of spectral properties that may be expected from compositional variations in lunar mineral samples. The sample names were chosen to reflect both mineral type as well as important information about mineral composition, and are as follows: a magnesian olivine, $Olv1_{Fo91}$ (Fo = molar (Mg/(Mg+Fe)*100)); a higher-Fe intermediate olivine, $Olv2_{Fo47}$; an orthopyroxene, Opx_{Mg88} (Mg = molar (Mg/(Mg + Fe)*100)); a diopside, $Diop_{En46}$ (En = molar (Mg/(Mg+Fe+Ca)*100)); and two Mg-spinels, $Sp1_{Mg98}$ and $Sp2_{Mg87}$. Brief descriptions of the samples are given in Table 1, and major element compositions are shown in Table 2. The compositions and spectral properties of the mafic silicate endmembers are discussed in the section below, followed by a description of the two spinel endmembers.

3.3.1. Mafic silicate endmembers.

The mafic component of lunar anorthosites is typically dominated by low-calcium pyroxene, although olivines and high-calcium pyroxenes do sometimes dominate the small mafic fraction (see Dymek et al. 1975; and Warren and Wasson 1977; James, 1980; McGee 1993). The compositions of these mafic minerals in lunar anorthosites are typically more ferroan, (~Mg40-Mg70) than the mafic component of the Mg-suite rocks (e.g., Dixon and Papike 1975; Ryder and Norman 1978; Warren and Wasson 1980; James et al. 1989; Warren 1990; McGee 1993; Warren 1993), which constitute the other major compositional grouping among pristine nonmare materials. The compositions of the olivines and low-calcium pyroxenes found in anorthosites and Mg-suite rocks are plotted in Figure 4, after Warren and Wasson (1979). For comparison, the olivine and orthopyroxene compositions used in this study are shown as horizontal lines, and generally bracket the range of compositions observed in the lunar samples. While the samples typically reveal a separation in Mg numbers between the Mg suite and the anorthositic rocks in Figure 4, assessing the extent to which this observations is representative of the global lunar crust requires understanding how these compositional differences are expressed in mixtures with high plagioclase abundances.

The two pyroxene samples used in this study were obtained from Ward's Science, and include an orthopyroxene from Bamble, Norway, and a diopside from Madagacar, both of which are highly magnesian (Tables 1 and 2). Due to the unavailability of a pure low-calcium pyroxene sample with intermediate Mg number, which would provide the best compositional and spectral analog for pyroxenes in most lunar anorthosites, the diopside was substituted to investigate the effects of occasionally-dominant high-calcium pyroxenes, particularly with respect to the changing 1000 and 2000 nm absorption band position. Spectra of the two pyroxene samples (Fig. 5b) are indeed dominated by broad absorption bands near 1000 and 2000 nm, although the center positions of these bands differ by ~200 nanometers which will provide important spectral variability when mixed with plagioclase. Impurities in the orthopyroxene sample were suggested to be tremolite by Singer (1981), and are likely the cause of the subtle sharp features near 1400 and 2300 nm. The least visibly altered grains of the diopside were selected for analysis, although similar sharp absorptions at long wavelengths, in addition to the broad feature near 700 nm, suggest that some impurities remain.

The two olivine endmember samples used in this study also differ substantially from one another in terms of their spectral properties as a result of differences in Mg number. The $\mathrm{Olv1}_{\mathrm{Fo91}}$ endmember is a sample of highly magnesian San Carlos olivine. Minor inclusions, presumed to be spinel or chromite, were removed upon crushing (Table 1). Spectra of this sample are shown in Figure 5a, and demonstrate a three-part composite absorption band centered near 1000 nm. The second olivine endmember, $\mathrm{Olv2_{Fo47}}$, is derived from a sample of the Kiglapait intrusion and is much more iron rich than the San Carlos sample (Tables 1 and 2). The olivine was manually separated from a bulk rock that also contained pyroxene and plagioclase, and was further purified using a magnetic separator. Due to the high iron content of $\mathrm{Olv2_{Fo47}}$, each of the individual absorptions comprising the bulk ~1000 nm feature shifts to slightly longer wavelengths and the intensities of each band also increases. However, extensive previous laboratory studies have demonstrated that these changes in the band characteristics do not occur at equal rates for each of the three absorptions. In particular, the M1 bands (outer absorptions) shift to a greater degree than the central M2 band. At the same time, the M1 bands increase in relative intensity compared with the M2 feature (e.g., Burns, 1970; Sunshine and Pieters, 1998; King and Ridley, 1987). The combined effects of these changes produce a composite absorption that visually appears broader and more flat-bottomed as the contrast between the three individual bands decreases and the long-wavelength shoulder becomes more pronounced with increasing iron abundance. We note also that the broad absorption between 2000 and 3000 nm in the spectrum of $\mathrm{Olv2_{Fo47}}$ (Fig. 5a) is likely due to very minor quantities of spinel inclusions, or possibly adhering pyroxene.

Analysis of returned lunar ferroan anorthosites suggests that although most contain relatively ferroan olivines that are more analogous to $\mathrm{Olv1_{Fo47}}$, examples of more forsteritic compositions do occur (e.g., anorthosite sample 76335, Warren and Wasson 1977). Furthermore, the primitive nature of high-Mg dunites makes their identification on the lunar surface an important objective in lunar science, and the high degree of overlap of olivine absorptions with the plagioclase absorption calls for an understanding of how much plagioclase could be "hidden" in spectra resembling pure, even forsteritic, olivine. These types of data are necessary to distinguish whether spectra resembling olivine could represent anorthositic lithologies rather than troctolites or dunites, which would each require very different petrogenetic interpretations (e.g., Yamamoto et al. 2010).

3.3.2. Spinel endmembers.

While spinel anorthosites have not been noted in the sample collection, recent remote sensing data have suggested their presence in numerous locations across the Moon's surface based on spectra that display spinel absorptions but lack absorptions due to olivine or pyroxene (e.g., Pieters et al. 2011; Pieters et al. 2013; Yamamoto et al., 2013). These exposures are generally found in feldspathic terrains, and are thought to contain a substantial amount of plagioclase. Although these spinel-bearing spectra also lack the diagnostic crystalline plagioclase absorption near 1250 nm, a large amount of plagioclase could be present in a "featureless" form in which the plagioclase absorption has been erased by processes of shock metamorphism (e.g., Adams et al. 1979; Johnson et al. 2003). Alternatively, the crystalline plagioclase absorption may simply be "hidden" by the strongly absorbing spinel component. The spectral characteristics of the remotely identified spinel are consistent with very high Mg numbers (>Mg90) (Jackson et al., in review). We have selected two aluminate Mg-rich spinel samples to independently mix with plagioclase in order to place constraints on the abundance of crystalline plagioclase that is necessary to generate a ~1250 nm absorption when in an intimate mixture with magnesian spinel. The two spinel samples are both highly magnesian but differ slightly in iron content and overall albedo. Sample $\mathrm{Sp1_{Mg98}}$ was chosen because it is a near-endmember magnesian composition and is highly pure (gem quality). Sample $\mathrm{Sp2_{Mg87}}$ was selected because a spinel from this locality (Amity, NY) was among the suite analyzed by Cloutis et al. (2004).

4. LABORATORY PROCEDURE

4.1 Sample processing

Preliminary processing steps unique to each endmember are described in Table 1. Once each sample was in particulate form, they were independently crushed in a Diamonite^{TM} mortar and pestle into several different size fractions: <45 µm, 45-75 µm, 75-125 µm, 125-250 µm, 250-500 µm, and 500-1000 µm. All size fractions except the finest were rinsed with de-ionized water after sieving to remove adhering fine particles. From these particle size separates, various binary mixture series were created using either a restricted particle size range (45-75 µm) or particle size distributions more typical of natural lunar soils (<1000 µm), both of which are described below. Excess material for each of the six particle size fractions of each mineral endmember are being made available in the RELAB for future studies. In all, 48 binary mixtures were prepared from the various mineral endmembers using the procedures described below.

4.2 Controlled particle size range

Because particle size is known to have a strong effect on albedo and absorption strength (e.g., Pieters 1983; Crown and Pieters 1987), we have controlled for this parameter in order to better isolate systematics due to mineral composition and abundance. The 45-75 µm particle size fraction was chosen specifically to maximize the overall spectral contrast so that variations in absorption characteristics are well expressed (e.g., Pieters 1983; Crown and Pieters 1987). To create mixtures with this restricted particle size range, the desired proportions of the 45-75 um fraction of both the plagioclase and non-plagioclase endmember were weighed out independently on a balance, then combined into a 4 mL glass vial and homogenized by tumbling and rotating for 5 minutes (mixtures with >5 vol% olivine, pyroxene, or spinel) or 10 minutes (mixtures with ≤5 vol% olivine, pyroxene, or spinel). This sequence was repeated using all six non-plagioclase endmembers in the following proportions (in terms of vol% olivine, pyroxene, or spinel): 2%, 5%, 7%, 10%, 15%, 25%, and 50%. We note that we have included in this study mixtures with proportions of non-plagioclase phases that would not be analogous to anorthosite, sensu stricto (15 vol%, 25 vol%, and 50 vol%). This was done intentionally for two reasons: (1) based on analysis of returned lunar samples, the plagioclase rich lunar crust very likely includes at least some areas that are slightly too mafic to be considered anorthosite (Warren 1990), and (2) to better elucidate the manner in which the plagioclase feature combines with other mineral absorption features and offer comparison to previous studies that have focused on lower plagioclase abundances (e.g., Mayne et al. 2010).

The total mass of each mixture varied slightly depending on the total amount of sample available, but was typically either 220 or 250 mg for the mixtures with >5 vol% of the non-plagioclase phase and 400 mg for mixtures with ≤5 vol% of the non-plagioclase phase. The extra sample for the mixtures with the lowest abundances of minor minerals was desirable so that at least 10 mg of each component would be present. Each of the mixtures were loaded into 9-mm diameter Teflon-coated sample dishes, except for the three mixtures containing ≥15% of Olv1$_{\mathrm{Fo47}}$, which were loaded into 5-mm dishes due to limited sample volume. We note that because the smaller dishes are also about half a millimeter more shallow, it's possible that some incident photons could have been absorbed by the inside of the dish after being transmitted through the olivine and plagioclase grains. This would have the effect of decreasing the overall brightness of the returned signal, although the results for these three samples (described below) do not suggest that this has a significant effect. The surface of the each sample was smoothed by gently passing the edge of a piece of weighing paper, angled at ~30 degrees, over the sample. Reflectance spectra of the six 45-75 μm mixture series and the additional six 0-1000 μm mixtures (described below) were acquired using the bidirectional reflectance spectrometer (BDR) in RELAB at Brown University, with an incidence angle of 30° and a 0° emergence angle (Pieters 1983).

The proportions of each endmember are expressed in terms of volume percent of solids rather than mass percent so that the weighting factor of each component can be considered analogous to the weighting factor given by Hapke (1981) for describing the bulk scattering properties of a linear combination of multiple components expressed in terms of single scattering albedo. For a two-component mixture, this weighting factor (f_1) for component 1 would be:

$$f1 = \frac{\frac{M_1}{\rho_1 D_1}}{\frac{M_1}{\rho_1 D_1} + \frac{M_2}{\rho_2 D_2}}$$

where M_1 is the bulk density $M_1 = N_1 \rho_1 D_1^3 (\pi/6)$, ρ_1 is the solid density, and D_1 is the diameter, and N_1 is the number of particles per unit volume for all particles of type 1 (Hapke 1981; Johnson et al. 1983; Mustard and Pieters 1987). If the particle sizes of the two components are assumed to be equal, the above equation for the weighting factor for component 1 reduces to the volume proportion of solids of component 1. To create the mixtures at the desired volume proportions (or weighting factor), the mass needed for each component was calculated from the target volume proportion (of solids), the desired total mass of the mixture, and the solid density of each component.

4.3 Particle size distributions

Because natural soils such as those collected from the lunar surface contain a distribution of particle sizes that vary largely as a function of surface maturity (e.g., McKay et al. 1974), it is important to also document the sensitivity of the mixture spectra to particle size variations in more realistic size distributions. Selected mixtures from the above set were duplicated using two different grain size distributions that both range from 0 to 1000 μm. The "coarse" distribution contains a higher proportion of large particles intended to represent relatively fresh, or texturally immature, surfaces on the Moon, such as steeply sloping crater central peaks. The "fine" size distribution contains a higher proportion of small particles and is intended to represent more texturally mature areas on the lunar surface that have been comminuted to a greater degree by micrometeorite bombardment and impact gardening.

Coarse and fine particle size distributions were prepared for each of the selected endmembers, and binary mixtures were then created by combining the mineral components (each consisting of a wide distribution of particle sizes) following the same method described above. The specific procedure is described schematically in Figure 6. For each "coarse" distribution mixture, both mineral components consist of <45 μm particles, 45-250 μm particles, and 250-1000 μm particles in the following proportions by weight: 20%, 30%, 50%, respectively. For the mixtures created with "fine" size distributions, the total mass of each component was divided into the same three size fractions, but in proportions of 50%, 30%, and 20%, respectively. The mass proportions of each size fraction that comprised the two distributions were selected to be generally consistent with the characterization of mature and immature lunar soils (<1 mm) described in McKay et al. (1972), Heiken et al. (1973), and McKay et al. (1974), although we note that they are not direct analogs due to the simplified nature of these pure two-component mixtures. After creating each endmember distribution, the two endmembers were combined in the desired total volume proportions. Each of these two distributions was created for mixtures of 93 vol% plagioclase plus 7 vol% of (1) $\mathrm{Olv1}_{\mathrm{Fo91}}$, (2) $\mathrm{Opx}_{\mathrm{Mg88}}$, and (3) $\mathrm{Sp1}_{\mathrm{Mg98}}$.

We emphasize that while these two particle size distributions mimic the size ranges for returned lunar soils, they are not direct analogs because they do not incorporate the additional optical effects of space weathering. Modification of lunar materials from extended exposure to the space environment is characterized by a range of complicated effects such as agglutinates and nanophase iron that have large consequences for bulk spectral properties (e.g., Pieters et al. 2000; Noble et al. 2007). Rather, the aim of these size distribution experiments is to illustrate the effects of natural particle size variations for comparison with the more restricted 45-75 μm binary mixtures.

5. RESULTS

5.1 Controlled particle size

5.1.1. General characteristics.

Near-infrared spectra of all six 45-75 μm mixture series are shown in Figure 7. These data demonstrate the spectral role of the plagioclase absorption in mixtures for which the bright, relatively transparent plagioclase component is present in high abundances. The results show that mixing small amounts of absorbing minerals with plagioclase results in an array of spectral characteristics that are unique to plagioclase-rich, mixtures.

Systematic variations in bulk absorption characteristics are clearly apparent as the type and proportion of the minor mineral changes. Within each series, an increase in olivine, pyroxene, or spinel abundance results in an increase in their respective absorption strengths, which is commonly associated with a decrease in overall albedo. Comparison of the different series in Figure 7 suggests that the “detectability” of the plagioclase 1250 nm absorption depends strongly on the identity of the coexisting minor minerals. Those with peak reflectance values that coincide with the wavelength range of the plagioclase absorption, such as Opx$_{Mg88}$ and Sp1$_{Mg98}$, are less effective at masking the plagioclase band. Olivines, by contrast, have absorptions that overlap with the plagioclase feature, making it more difficult to distinguish the contribution of plagioclase to the bulk spectrum, even at plagioclase abundances > 90 vol%.

In general, these results demonstrate two important characteristics of plagioclase-rich mineral mixtures: (1) the non-plagioclase endmembers exert strong influence on bulk spectra at low modal proportions, although important variations are apparent, and (2) despite the strong influence of other phases, *the plagioclase component does in fact affect the shape of most mixture spectra*, either by creating complex "composite" absorptions (for plagioclase abundances ≥90 vol%), or by subtly modifying the characteristics of the non-plagioclase endmember spectra (generally for mixtures with <90 vol% plagioclase). Below, we describe in more detail the varying spectral characteristics that arise from combining plagioclase with various amounts of different minerals.

5.1.2. Plagioclase mixed with ≤10% olivine, pyroxene, or spinel.

The varying effects of different minerals at a given modal proportion in plagioclase-dominated mixtures are compared in Figures 8 and 9. Just 2 vol% of any of the non-plagioclase endmembers exerts a visible effect on the bulk spectrum, although some endmembers are clearly more dominant than others (Fig. 8a). Mixtures containing 2 vol% of Olv1$_{Fo91}$, Olv1$_{Fo47}$, or Diop$_{En46}$ share similar spectral characteristics: in general, they resemble a wide, distorted plagioclase absorption. The 2 vol% Opx$_{Mg88}$ mixture, however, differs significantly from the other mafic silicates: 2 vol% of this strongly absorbing phase results in an orthopyroxene absorption near 950 nm that is nearly equal in strength to and distinguishable from the plagioclase absorption near 1250 nm. A subtle ~2000 nm orthopyroxene is also apparent at longer wavelengths. This overwhelming effect of the orthopyroxene supports previous observations (e.g., Nash and Conel 1974; Crown and Pieters 1987).

The different mafic silicates are more distinguishable from one another when present in 5-10 vol% abundance. At the 5 vol% level, the local minimum of the diopside endmember, centered near 1050 nm becomes apparent, as does a weak 2000 nm absorption. For mixtures containing the diopside endmember, the effect of the plagioclase absorption on the bulk spectrum progresses from being explicitly observable in the 2 vol% and 5 vol% mixtures to being expressed simply as a flattening of the reflectance maxima near 1250 nm in the 7 vol% and 10 vol% mixtures (Fig. 8 c,d). For mixtures with $\mathrm{Opx}_{\mathrm{Mg88}}$, a subtle plagioclase absorption is visually apparent superimposed on the pyroxene spectrum even when the pyroxene is present in up to 10 vol% abundance (Fig. 8 b-d). We note that this high sensitivity to the presence of plagioclase in the orthopyroxene mixtures would be mitigated if a 1200 nm M1 absorption were present in the pyroxene endmember spectrum, as would be expected for a more iron-rich orthopyroxene. This effect is described in more detail below and in Figures 17 and 18, although future work directed at the relationship between the 1250 nm plagioclase absorption and the 1200 nm M1 pyroxene absorption is necessary.

The two olivine endmembers are also distinguishable from the pyroxenes at the 5 vol% level, displaying a wide, almost flat-bottomed shape. The olivine-bearing mixtures are similar to one another between 5-10%, except that the enhanced ~850 nm M1 absorption in $\mathrm{Olv1}_{\mathrm{Fo47}}$ is subtly expressed in these mixtures. The result is that mixtures with $\mathrm{Olv1}_{\mathrm{Fo47}}$ display a broader absorption, one that extends below 1000 nm, than the mixtures containing $\mathrm{Olv1}_{\mathrm{Fo91}}$. This distinction is so pronounced and regular that we suggest it may be useful in distinguishing olivine compositions in remote sensing data for the Moon, although we caution that mixtures of plagioclase plus low abundances (≤5 vol%) of diopside may be indistinguishable from mixtures with forsteritic olivine. It is also important to note that, by visual inspection, the mixtures containing 5, 7, and 10 vol% $\mathrm{Olv1_{Fo47}}$ simply resemble the $\mathrm{Olv1_{Fo47}}$ endmember with subdued spectral contrast.

Spectra of mixtures containing 2 vol% of either spinel endmember display a characteristic negative slope resulting from the influence of strong 2000 and 3000 nm absorptions (Fig. 8a). The major difference between the two 2 vol% spinel mixtures is the strength of the plagioclase absorption near 1250 nm: addition of a darker, more iron-rich spinel ($\mathrm{Sp2_{Mg87}}$) subdues the plagioclase absorption more significantly. Mixing with a more transparent, very iron-poor spinel ($\mathrm{Sp1_{Mg98}}$) allows the subtle 1250 nm plagioclase absorption to persist even when the spinel represents more than 10 vol% of the bulk material (Fig. 9c, f, i). Importantly, the long-wavelength absorptions in the mixture containing 5 vol% $\mathrm{Sp1_{Mg98}}$ is more clearly resolved into two components, one centered near 2000 nm and the other near 3000 nm that is just beyond the wavelength coverage of the BDR measurements, than the corresponding 2 vol% mixture. This type of structure in the long wavelengths can be used to identify spinel in remote sensing data by distinguishing these absorptions from weak single-component "absorptions" that can result from instrumental effects (Pieters et al., *in press*).

5.1.3. Plagioclase mixed with > 10 vol% olivine, pyroxene, or spinel.

The spectral characteristics of mixtures containing 15, 25, and 50 vol% of the non-plagioclase phase increasingly resemble the non-plagioclase endmembers, although the effect of the plagioclase component is still subtly apparent in many cases (Fig. 9). A discrete plagioclase absorption is visually apparent for the mixture containing 15 vol% $\mathrm{Sp_{Mg98}}$. However, for most other mixtures containing more than 10 vol% of a non-plagioclase phase, the spectral influence of plagioclase is typically expressed primarily as either (1) a flattening of ~1250 nm reflectance maxima in pyroxene or spinel dominated spectra, or (2) the broadening of the ~1000 nm absorption in olivine dominated spectra. The "flattening' effect in particular has been previously described by Crown and Pieters (1987) for mixture of plagioclase and orthopyroxene (the same magnesian orthopyroxene used here) at varying particle size fractions. At the 50% level, the only mixtures that are most visually distinguishable from the more absorbing endmember, are $\mathrm{Opx_{Mg88}}$ and the $\mathrm{Sp1_{Mg98}}$. For these two endmembers, the reflectance maximum near ~1250 nm is simply flattened.

5.1.4. Measuring relative band depths.

We have developed a parameter specifically to quantify relative absorption depths of the different components in a plagioclase-dominated mixture, which is an important indicator of mineral abundance. While a similar parameter may be developed for characterizing remote observations of mixture spectra, we caution that direct application of the parameter values described here to the remote sensing case is inappropriate until various effects such as space weathering and particle size are accounted for. Rather, the aim of parameterizing the laboratory data here is to better elucidate the systematic spectral changes brought on by varying endmember composition and abundance – beyond what is visually apparent. We focus on mixtures with the mafic silicates, which have absorptions near 1000 nm that may overlap somewhat with the ~1250 nm plagioclase absorption.

The relative absorption depths of the plagioclase and mafic silicate components can be characterized by comparing the minimum reflectance values in the ~1000 and ~1250 nm regions in a given spectrum. To make this comparison, we find the minimum reflectance value between 850-1050 nm for each spectrum after removing a linear continuum that is tied at the reflectance maxima between 550-900 nm (short-wavelength tie-point) and between 1350-1900 nm (long-wavelength tie point). The slope of a line anchored by the reflectance minimum between 850 - 1050 nm and the reflectance value at 1250 nm is used to compare the relative plagioclase and mafic absorption depths for all spectra. A schematic of this relative band depth parameter applied to an olivine spectrum is shown in Figure 10. For a given series, higher proportions of mafic minerals correspond to more positive slope values.

A comparison of the relative plagioclase – mafic absorption depths calculated using the parameter described above is shown in Figure 11. For all four series, most of the change in relative band depths occurs with the addition of <15 vol% mafics. This observation illustrates that anorthosites represent an important compositional range in which small changes in mineralogy represent large changes in bulk spectral properties. Further, it is apparent that both of the pyroxene mixture series (1) reach significantly higher slope values (e.g., stronger mafic absorptions relative to the plagioclase absorption) than the olivine series, and (2) show continued change in the relative mafic-plagioclase absorption strengths (or, slope parameter) even for high pyroxene abundances.

These observations reveal an important difference in the manner in which the plagioclase absorption combines with the absorptions of these two types of common mafic minerals. Specifically, because the plagioclase band does not overlap with the primary absorptions of the pyroxene endmembers used here, the addition of this pyroxene component weakens the absolute strength of the absorption near 1250 nm while at the same time increasing the strength of the pyroxene absorption near 1000 nm. Olivines, by contrast, have an absorption that overlaps with the plagioclase feature. As a result, the 1250 nm region in an olivine – plagioclase mixture represents contributions from both mineral components. Further, and most importantly, it is clear that while pyroxenes are much more optically dominant than olivines, the lack of overlap of the plagioclase and pyroxene absorption bands means that the relatively weak plagioclase component is more distinguishable and actually exerts a more noticeable influence on pyroxene-dominated spectra than on olivine-dominated spectra. The large degree of overlap with olivine absorptions, by contrast, results in a plagioclase band that is easily hidden within olivine-dominated spectra. The relatively strong influence of the plagioclase absorption on pyroxene-dominated spectrum is expected to be mitigated if the pyroxene spectrum itself contains a ~1200 nm absorption due to iron in the M1 crystallographic site (typical for iron or calcium rich compositions, or disordered pyroxenes) (e.g., Klima et al. 2007, 2008). Clearly the mixing behavior of plagioclase and these types of pyroxenes is an important avenue of study, which is touched upon only briefly in following sections (see Figures 17 and 18) and should be elaborated on in future work.

5.2 Particle size distributions

The general characteristics of plagioclase-rich mixtures described above are preserved even for particle size distributions relevant to natural lunar soils. Mixtures of plagioclase with 7% mafics are used for these analyses, and their spectra are shown in Figure 12. Soil mixtures with a high proportion of fine particles (mature) have a higher albedo than the mixtures with a higher proportion of large particles (immature) (Fig. 12a-c). The albedo of the corresponding 45-75 µm mixtures generally falls between the two analog soil distributions. Spectra of these mixtures that are scaled to unity at the wavelength of maximum reflectance for the 45-75 µm mixture are shown in Figure 12 d-f. Although small variations in absorption depths are apparent, the immature and mature particle size distributions are on the whole very similar to each other. The 45-75 µm fraction typically displays slightly greater overall spectral contrast.

We note, however, that the effect on relative absorption strengths in bulk mixture spectra would be greater if the each component each had a different particle size distribution. Indeed, the spectral consequences of a strongly absorbing component that is physically smaller on average than the plagioclase component, as is the case for typical lunar anorthosites in the sample collection (e.g., McGee 1993), is an important avenue for further study.

6. NONLINEAR MIXING MODEL

6.1 Non-linear mixing model background

While systematic laboratory analyses across a wide compositional space can provide highly accurate information about mixture spectra, they are impractical in many circumstances. Such analyses using returned lunar samples as endmembers, for example, are not ideal because of the relatively large volume of sample that must be consumed. Models that accurately predict how mineral absorptions combine to create a bulk mixture spectrum are therefore desirable in order to understand the range of spectral characteristics that might characterize a surface of unknown composition. Ultimately, mixing models have wide applicability for estimating the mineral abundances represented in a remotely acquired reflectance spectrum.

Laboratory mineral mixtures are often used to validate such models aiming to predict mineral abundances in a given reflectance spectrum comprised of intimately mixed components (e.g., Johnson 1983; Mustard and Pieters 1987, 1989). Non-linear models must be used to account for the disproportional contribution from highly absorbing components that arises when light interacts with a number of particles before returning to the sensor. Here, we use the well-characterized mixture spectra generated for this study to test the ability of the Hapke model (Hapke 1981, 1993, 2002) to predict the reflectance spectrum of each mixture based on the endmember spectra. Specifically, we are interested in determining how well the mixture spectra can be predicted for this highly non-linear regime in which the bright, relatively transparent plagioclase component is an important contributor to the bulk spectrum.

The Hapke approach is based on relating reflectance values of each endmember and mixture spectrum to a parameter called single scattering albedo (SSA), which depends only on the absorption characteristics of individual minerals. The relationship between reflectance and SSA is highly non-linear. However, once converted to SSA, each spectrum can be expressed as a linear combination of endmembers, at each wavelength, weighted by the factor, *f*, (defined above). Here, we have assumed that the two prepared endmembers have the same particle size (wet-sieved to 45-75 μm), and so the weighting factor can be approximated by volume fraction.

6.2 Inverse model

We first use an inverse model to calculate a best-fit spectrum to each laboratory mixture using the appropriate measured endmember spectra as inputs. For a given mixture series (seven mixtures and two endmembers), each reflectance spectrum was converted into SSA using a look-up table constructed from equation 37 of Hapke (1981) at a step size of 10^{-4} in SSA. We have assumed an isotropic phase function, a backscattering term of zero, and implement the Hapke (2002) H-function approximations to account for multiple scattering. For each SSA mixture spectrum, the best-fit linear combination of endmember SSA spectra, weighted by the factor, *f*, was found by minimizing the least-squares error. The proportions of each endmember for the best-fit spectrum were constrained to be non-negative and normalized to one. The resulting best-fit modeled spectra were converted back to reflectance (technically, radiance coefficient) for comparison with the laboratory prepared spectra (Hapke 1981).

The best-fit modeled spectra are shown compared with the corresponding laboratory prepared spectra in Figure 13. The proportions of each endmember modeled for each best-fit

Always consult and cite the final, published document. See http://www.minsocam.org or GeoscienceWorld

spectrum are given in Table 3. In general, the modeled spectra are good approximations to the laboratory prepared spectra, and the modeled endmember proportions match the prepared abundances to within <10 vol% for all mixtures in all series. The best-fit spectra for all anorthosite-like mixtures (containing ≥90% plagioclase) matched the prepared abundances the most closely, to within 5 vol%. The abundances of the non-plagioclase component for each modeled mixture spectrum are compared with the true prepared abundance in Figure 14. The series that produced the best estimation of mineral abundance overall was the orthopyroxene, and all other modeled series predicted slightly higher proportions of the minor minerals than expected for the laboratory mixtures. Residual spectra calculated by subtracting the best-fit modeled spectrum from the laboratory prepared spectrum for a given mixture in reflectance space, are given in the Appendix. Many of the residual spectra do show “structure”, above the level of the noise, indicating that the model is not able to fit each mixture spectrum with a linear combination of the endmembers in SSA space for all examples. However, it appears that neither the plagioclase nor the non-plagioclase endmembers are systematically over- or under-estimated in the residuals, and some discrepancy could arise from laboratory measured sample characteristics as well.

To illustrate differences in the relative absorption depths between measured and modeled spectra, the slope parameter, described above and in Figure 10, was calculated for the modeled olivine and pyroxene spectra. The same continuum removal procedure was applied to the modeled spectra prior to this calculation. A comparison of the relative absorption band depths for the measured versus modeled mixtures is shown in Figure 15. For the mixtures containing higher mafic abundances (Fig. 15a) most of the modeled spectra, with the exception of the orthopyroxene series, appear displaced to higher slope values than the measured mixtures, indicating relatively stronger mafic bands. This effect is small, however, and not generally discernable by inspection of the spectra in Figure 13. For mixtures containing ≥90 vol% plagioclase (Fig. 15b), both of the olivine series display higher discrepancies between measured and modeled relative absorption depths. The relative absorption depths in the modeled $\mathrm{Opx}_{\mathrm{Mg88}}$ and $\mathrm{Diop}_{\mathrm{En46}}$ series are more consistent with the measured spectra.

6.3 Forward model

We have also used the laboratory mixtures to validate a forward model based on the Hapke approach. The specific advantage of a forward model is the ability to calculate a mixture spectrum from any two input endmembers. This allows characterization of mixtures that consist of endmembers with different compositions or spectral properties than were available for the laboratory mixtures.

To produce the forward modeled mixtures, the measured reflectance spectrum of each endmember was converted to SSA using a look-up table as done for the inverse model. The endmembers (expressed in SSA) were then combined linearly in the same proportions as the measured laboratory mixtures (2, 5, 7, 10, 15, 25, and 50 vol%). The resulting mixture spectra were converted back to reflectance using the same procedure described above for the inverse model. The modeled spectra produced in this manner are shown with the corresponding laboratory mixtures in Figure 16.

For the olivines and the $\mathrm{Diop}_{\mathrm{En46}}$ series, the modeled mixtures are typically offset slightly toward higher reflectance across the composite absorption features between ~1000 and 1500 nm (Fig. 16 a,b,d). The visibly largest discrepancy between measured and modeled spectra occurs for the mixtures containing $\mathrm{Olv1}_{\mathrm{Fo47}}$ endmember at proportions >10 vol%. The orthopyroxene-bearing mixtures were modeled the most accurately.

6.4 Modeling variations in pyroxene composition

We can take advantage of this forward modeling approach to more fully address how mineral composition affects the spectra of plagioclase-dominated mixtures. For instance, the pyroxene endmembers used in the laboratory prepared mixtures are more magnesium-rich than most pyroxenes found in lunar anorthosites. It will be important to better understand the spectral characteristics of mixtures with more iron-rich pyroxenes in particular because they typically display weak absorption bands centered near 1200 nm, which overlap with the plagioclase ~1250 nm absorption, due to excess iron in the octahedral M1 site (e.g., Klima et al, 2007). In addition, because relative Mg and Fe contents are expected to have an effect on pyroxene absorption strength, it is worthwhile to explore the magnitude of this effect on mixture spectra.

Using as endmembers a suite of four synthetic orthopyroxenes that vary systematically in iron content (Klima et al. 2007), we calculate model mixtures with the same terrestrial plagioclase endmember as in the laboratory mixtures. Spectra of the synthetic orthopyroxene endmembers, obtained from the RELAB database, are shown in Figure 17. These endmembers were specifically chosen span a wide range of iron and magnesium abundances: En90, En70, En50, and En30. The En70 and En50 samples are most compositionally analogous to the low calcium pyroxenes found in lunar anorthosites. While the addition of iron across this sample suite does generally cause an increase in ~1000 and ~2000 nm absorption strength, which are primarily due to iron in the M2 octahedral site, other effects highlight the fact that iron also partitions onto the M1 site at higher abundances, giving rise to (1) a broadening of the ~1000 nm absorption, and (2) a strengthening of the ~1200 nm absorption relative to the ~1000 and ~2000 nm absorptions. The spectral contrast in the highest- FeO sample is also notably depressed. We caution that these synthetic pyroxenes and the mixtures produced below should not be compared directly to the laboratory prepared series described above, primarily due to the small grain size of the synthetics resulting in reduced spectral contrast, as well as the relatively fast cooling rate that likely enhances the ~1200 nm pyroxene absorption. Thus, this analysis aims only to qualitatively demonstrate the magnitude of the effect of varying pyroxene composition when all other variables are held constant.

The modeled mixtures produced using these endmembers plus the natural plagioclase are shown in Figure 18, for mixtures with ≥90% plagioclase. There are a number of characteristics that are immediately apparent. First, the spectral properties of orthopyroxenes with very high iron abundances (here, En30), namely a broadened ~1000 nm band and a pronounced 1200 nm feature, are distinct even when the orthopyroxene endmember is present in ≤10 vol% abundance. Thus, although very iron-rich pyroxenes aren't expected to dominate the mafic component of lunar anorthosites, their presence likely would be obvious at near-infrared wavelengths, even when high abundances of plagioclase are present. For the modeled mixtures containing orthopyroxenes with more intermediate compositions (En70 and En50), spectral characteristics are similar to the laboratory mixtures containing a magnesian orthopyroxene, and are dominated by composite features resembling a "w" shape. The relatively dominant plagioclase absorption in modeled mixtures containing the En90 orthopyroxene underscores the strong sensitivity of near-infrared spectra to sample texture: approximately the same pyroxene compositions was used in the laboratory mixtures shown in Figure 7c, but the pyroxene absorption in Figure 18 is much weaker owing to its smaller grain size.

In general, the variations in pyroxene composition explored in this modeling exercise cause spectral changes that are similar in magnitude to a few percent variation in pyroxene abundance. While it is therefore difficult to isolate the individual effects of pyroxene composition and abundance using only the spectral characteristics of the 1000-1500 nm wavelength region, we suggest that additional leverage may come from examination of the ~2000 nm absorptions in these mixture spectral. For instance, an important result from the modeled mixtures in Figure 18 is that the increase in the position of the ~2000 nm absorptions with increasing iron content is readily apparent, even when the pyroxene component is present in ≤10 vol% abundance. Therefore, using a combination of the ~2000 nm band position and the spectral characteristics of the ~1000-1500 nm region, it may be possible to better disentangle the spectral effects of pyroxene composition and abundance in reflectance spectra.

7. DISCUSSION

Far from being a spectrally unimportant component of mafic- or spinel-bearing mixtures, the results of the laboratory and modeling analyses demonstrate that plagioclase can be a significant contributor to bulk spectral properties, particularly when present in the high abundances relevant for the lunar crust. This study has focused on a plagioclase endmember that displays a prominent 1250 nm absorption, as has recently been observed by remote spectrometers measuring the Moon’s crust (e.g., Pieters et al. 2009; Ohtake et al. 2009; Yamamoto et al. 2012; Donaldson Hanna et al. in review). When the 1250 nm absorption is present, addition of small quantities of olivine, pyroxene, or spinel results in a diverse suite of spectral properties that (1) are unique to plagioclase-rich mixtures, (2) vary systematically according to type and proportion of the non-plagioclase phase, and (3) can be modeled accurately using non-linear approaches.

The “composite” absorptions between ~1000 and ~1500 nm that characterize mixtures with very small proportions of olivine and pyroxene (Fig. 8) are unique to materials with anorthositic proportions of crystalline plagioclase. While the relative plagioclase – mafic absorption depths documented in this study should not be considered diagnostic for remotely measured lunar materials at this stage, the results suggest that pyroxene and olivine are generally distinguishable from one another even when present in small abundances. Furthermore, large differences in olivine or pyroxene composition also appear to be discernable. For instance, the position of the ~2000 nm pyroxene absorption, which is highly diagnostic of Fe and Ca content, differs by several hundred nanometers in the pyroxene endmembers investigated here (Fig. 5b). This difference is apparent even when the pyroxene is only present in less than 10% abundance.

The results of this study also suggest that the plagioclase absorption can have a subtle effect on mixture spectral properties even when more strongly absorbing minerals, particularly magnesian orthopyroxenes and spinels, are present in >10% abundance (Figure 9). However, at these lower plagioclase abundances, particularly close to 50% plagioclase, this effect is largely manifested as a decrease in spectral contrast and an increase in albedo, rather than an explicit plagioclase absorption. Since both spectral contrast and overall albedo can be strongly affected by various other parameters, such as sample texture and grain size, it is unlikely that this information could be used to uniquely identify plagioclase at proportions near 50%. This is indeed suggested by previous studies that have investigated spectral mixtures with ~50% plagioclase and have not found unique evidence for a plagioclase component expressed in spectral absorption characteristics (e.g. Mayne et al. 2010). We also emphasize that the laboratory study presented here has focused on binary mixtures, but if a third component were present, such in the form of a two-component pyroxene, some of the spectral effects plagioclase could be further suppressed at these lower plagioclase abundances. The use of non-linear forward models, like those described in previous sections, will be a useful tool for exploring the limits of plagioclase detectability for a wider range of natural samples.

The observations of spinel-bearing mixtures also have potential implications for interpreting remotely acquired spectra of the lunar crust. For instance, recent M^3 and Spectral Profiler spectra displaying spinel absorptions in the absence of mafic features point to a new lunar rock type (e.g., Pieters et al. 2011; Yamamoto et al. 2013). These materials are typically found in feldspathic areas and are believed to consist of a large proportion of plagioclase, the amount of which is still relatively unconstrained. No plagioclase absorption is observed in these remote data, which could be due either to (1) the effects of shock metamorphism preferentially destroying the plagioclase crystal structure necessary to generate the ~1250 nm absorption (e.g., von Engelhardt and Stöffler 1968; Stöffler 1971;Adams et al. 1979), or (2) spinel being present in sufficient quantities to mask a crystalline plagioclase absorption. Although a host of factors such as space weathering effects and sample texture prohibit direct comparison of our mixture samples with the lunar data, the mixtures examined here can begin to address the question of how much spinel is necessary to mask plagioclase bands. Examination of the spinel mixture data in Figures 7-9 shows that the ability of a spinel to "hide" a plagioclase absorption is highly dependent on the spinel composition. A dark, highly absorbing spinel in our samples needs only to be present in 5% abundance in order to mask the crystalline plagioclase band. The same plagioclase absorption, however, is still discernable in the mixtures containing 15 or 25% of a more transparent spinel.

While the detailed mixing systematics described in preceding sections are only strictly relevant to a controlled set of experiments that is necessarily limited in the compositions and abundances explored, the validation of the Hapke nonlinear modeling approach provides leverage for continuing to explore the more complex set of conditions that characterize lunar materials. The results have shown that the model works best for describing mixture spectra in which both the plagioclase and minor mineral absorptions exert a measurable effect on spectral properties, namely when the abundance of the more absorbing component is low (≤10%) and when the plagioclase and mafic absorptions do not overlap substantially. In future work, the forward modeling approach can be used to calculate mixtures using as endmember spectra returned lunar samples, or experimental samples that that have experienced varying degrees of space weathering or shock metamorphism.

8. APPLICATION

The analyses above provide a framework for estimating which minor phases may be contributing to plagioclase-dominated spectra, even if textural and compositional differences from natural lunar materials prohibit precise quantification of mineral abundances at this time. Representative M^3 spectra from three different regions are shown in Figure 2. For each region, we identify areas that resemble relatively pure plagioclase (Fig. 2a), areas that display composite absorption features between 900 and 1500 nm (Fig. 2b), and areas with spectra dominated by a mafic component with absorptions near 1000 nm (Fig. 2c).

The examples from the Orientale basin have been discussed in detail in Cheek et al. (2013). In general, they represent a clear progression from a pure plagioclase component (Fig. 2a) to spectra containing two distinguishable absorptions that are comparable to the mixtures of plagioclase plus small amounts of orthopyroxene described in Figures 8 and 18 (Fig. 2b). These types of composite absorptions are analogous to the Class B spectra in Cheek et al. (2013). The more mafic-dominated spectrum shown for Orientale in Figure 2c is unlikely to be a pure orthopyroxene, rather the “flattening” of the spectrum in the 1250 nm region indicates that more than a few percent plagioclase is present (e.g., Figure 8 b-d, 9).

At Copernicus, spectra resembling pure plagioclase are observed in restricted areas in the northern wall (Fig. 2a). In addition, a number of locations in the central peaks and walls strongly resemble spectra of forsteritic olivine (e.g., Pieters 1982; Yamamoto et al. 2010). These spectra are consistent with troctolite or dunite and have been interpreted to suggest that either deep-seated crustal material in the form of Mg-suite plutons or mantle material have been exposed by the Copernicus impact. Close inspection with M^3 data, however, reveals that a few small areas within the central peaks display spectra with composite flat-bottomed absorptions (Fig. 2b) that could represent a combination of the plagioclase feature and olivine. These exposures are on the order of a few hundred meters and are likely too small to have been detected with telescopic data. We have shown that these types of flat-bottomed absorptions are characteristic of laboratory mixtures containing plagioclase plus small amounts of a magnesian olivine (Fig. 8). For the Copernicus example, the limited geologic extent of these composite absorption features within the crater suggests that they could represent relatively localized regions of enhanced plagioclase abundance in a layered pluton containing olivine. This interpretation is supported by the high Mg content suggested for the olivine component by the narrow extent of the flat-bottomed absorption.

The origins of the spectral features in the central peak of Tsiolkovskiy crater are more ambiguous. A number of locations within the peak display strong absorptions that resemble plagioclase, but are likely too broad to be considered as pure as the examples at Orientale and Copernicus (Fig. 2a). Most of these plagioclase-like spectra also display weak 2000 nm absorptions, suggesting the presence of small amounts of pyroxene or a spinel-bearing olivine. Although Tsiolkovskiy displays a wide range of spectral characteristics throughout the central peak, one of the clearest examples of a mafic-dominated component is a pyroxene-dominated spectrum shown in Figure 2c. The example shown in Figure 2b (continuum-removed in 2e) represents a few exposures within Tsiolkovskiy's central peak that display spectra with a broad, flat-bottomed shape. These spectra are distinguished from the flat-bottomed spectra in Copernicus, however, by the fact that the absorption covers a spectral range that extends below 1000 nm and a distinct absorption near 2000 nm is observed. This type of wide, completely flat composite absorption, with an associated 2000 nm absorption is not observed in any of the binary laboratory mixtures presented in this paper. We suggest that this type of composite absorption may represent a mixture for which three different mineral components are spectrally significant, such as olivine, pyroxene, and plagioclase, or alternatively some absorbing component not considered here, such as a glass or a two-pyroxene mixture, both of which have somewhat broad primary absorption features. The spectral characteristics of the Tsiolkovskiy central peak are under investigation to better constrain the spatial distribution of mineralogic signatures in M^3 data.

9. IMPLICATIONS

Prior to the identification of the 1250 nm plagioclase absorption across the lunar surface, the mineralogy of the Moon's primitive anorthositic crust was largely invisible to near-infrared spectrometers. Now that these anorthosites are accessible for evaluation, describing their global compositional diversity hinges on an ability to distinguish the signatures of different co-occurring minor minerals within a plagioclase matrix and make estimates about variations in their relative abundances. This study has been directed at demonstrating the various effects of composition (Fo, En, or Mg number) and abundance of olivine, pyroxene, and spinel on plagioclase-dominated reflectance spectra using the simplest, purest endmembers. The major findings demonstrate that:

(1) Plagioclase is not simply a featureless high-albedo component in all cases, but one that exerts measurable control on bulk spectral properties, particularly when present in high abundance;

(2) Plagioclase-mafic composite absorptions that are observed in spectra of mixtures containing ≤10% olivine or pyroxene are diagnostic of anorthosite-like mixtures. However, their individual characteristics depend on the type and composition of the mafic mineral;

(3) Plagioclase is easily "hidden" by a few percent olivine because the major absorptions of each mineral overlap substantially. Some pyroxene and very high-Mg spinel spectra, however, are highly distorted by the presence of plagioclase across a wider range of mixture proportions;

(4) For the mixtures explored here, those containing >10 vol% olivine, pyroxene, or spinel generally resemble spectra of these endmembers by visual inspection. This observation emphasizes the importance of using caution when interpreting remote sensing NIR spectral data that do not display explicit evidence for a plagioclase absorption;

(5) Nonlinear models can accurately predict mineral abundances in anorthosite-like mixture spectra to within 5 vol%. This validation of the nonlinear modeling approach for mixtures containing an abundant high-albedo component enables further investigation of the range of spectral characteristics expected for lunar anorthosites through the use of different endmembers than those specifically investigated here.

Always consult and cite the final, published document. See http://www.minsocam.org or GeoscienceWorld

While a number of other factors such as the space weathering of lunar surface materials invariably complicate the applications of these data for remotely sensed anorthosites, the well-controlled, systematic dataset produced here provides a framework for developing applications to more complex remotely acquired spectra such as those observed at Orientale, Copernicus, and Tsiolkovskiy.

ACKNOWLEDGMENTS

We are grateful for support of this project from the NASA Lunar Science Institute (#NNA09DB34A). Thanks to Taki Hiroi for his immense help getting all of the laboratory mixtures measured in RELAB, and to Ralph Milliken and Tim Goudge for generously providing much of the Hapke mixing codes. Colin Jackson was also a great help in acquiring the mineral endmembers.

REFERENCES CITED

Adams, J.B., and McCord, T.B. (1970) Remote sensing of lunar surface mineralogy: Implications from visible and near-infrared reflectivity of Apollo 11 samples, Proceedings of the Apollo 11 Lunar Science Conference, 1937-1945.

Adams, J.B., and Goullaud, L.H. (1978) Plagioclase feldspars: visible and near infrared diffuse reflectance spectra as applied to remote sensing, Proceedings of the 9th Lunar and Planetary. Science. Conference, 2901-2909.

Adams, J.B., Hörz F., and Gibbons, R.V. (1979) Effects of shock-loading on the reflectance spectra of plagioclase, pyroxene, and glass, Lunar and Planetary Science Conference, 10th, 1-3.

Bell, P.M., and Mao, H.K. (1973) Optical and chemical analysis of iron in Luna 20 plagioclase, Geochimica et Cosmochimica Acta, 37, 755-758.

Bruckenthal, E.A., and Pieters, C.M. (1984) Spectral effects of natural shock on plagioclase feldspar, Lunar and Planetary Science Conference, 15th, 96-97.

Burns, R. G. (1970) Crystal field spectra and evidence of cation ordering in olivine minerals, American Mineralogist, 55, 1608-1632.

Burns, R. G. (1974) The polarized spectra of iron in silicates: Olivine. A discussion of neglected contributions from Fe^{2+} irons in M(1) sites, American Mineralogist, 59, 625-629.

Burns, R. G. (1993) Mineralogical Applications of Crystal Field Theory, 2nd ed., 551 pp., Cambridge Univ. Press, New York.

Cheek, L.C., and Pieters, C.M., (2012) Variations in anorthosite purity at Tsiolkovsky crater on the Moon, Lunar and Planetary Science Conference, 43rd, Abstract 2624.

Cheek, L.C., Donaldson Hanna, K.L., Pieters, C.M., Head, J.W., and Whitten, J.L. (2013) The distribution and purity of anorthosite across the Orientale basin: New perspectives from Moon Mineralogy Mapper data, Journal of Geophysical Research - Planets, 118, 1805-1820.

Cloutis, E.A., and Gaffey, M.J. (1991) Pyroxene spectroscopy revisited: Spectral- compositional correlations and relationship to geothermometry, Journal of Geophysical Research - Planets, 96, 22809-22826, doi:10.1029/91JE02512.

Cloutis, E.A., Sunshine, J.M., and Morris, R.V. (2004) Spectral reflectance-compositional properties of spinels and chromites: Implications for planetary remote sensing and geothermometry, Meteoritics and Planetary Science, 39, 545-565.

Conel, J.E., and Nash, D.B. (1970) Spectral reflectance and albedo of Apollo 11 lunar samples: Effects of irradiation and vitrification and comparison with telescopic observations, Proceedings of the Apollo 11 Lunar Science Conference, 3, 2013-2024.

Crown, D.A., and Pieters, C.M. (1987) Spectral properties of plagioclase and pyroxene mixtures and the interpretation of lunar soil spectra, Icarus, 72, 492-506.

Deer, W.A., Howie, R.A., and Zussman, J. (1992) An introduction to the rock-forming minerals, 696 p., Addison-Wesley-Longman, Reading, MA.

Dhingra, D., Pieters, C.M., Boardman, J.W., Head, J.W., Isaacson, P.J., and Taylor, L.A. (2011) Compositional diversity at Theophilus Crater: Understanding the geological context of Mg-spinel bearing central peaks, Geophysical Research Letters, 38, L11201.

Dixon, J.R., and Papike, J.J. (1975) Petrology of the anorthosites from the Descartes region of the Moon: Apollo 16, Proceedings of the 6th Lunar and Planetary Science Conference, 263-291.

Donaldson Hanna, K.L., Cheek, L.C., Pieters, C.M., and Mustard, J.F., Global assessment of pure crystalline plagioclase across the Moon and implications for evolution of the primary crust, Journal of Geophysical Research - Planets, In Review.

Dymek, R.F., Albee, A.L., and Chodos, A.A. (1975) Comparative petrology of lunar cumulate rocks of possible primary origin-Dunite 72415, troctolite 76535, norite 78235, and anorthosite 62237, Proceedings of the 6th Lunar and Planetary Science Conference, 301-341.

Elkins-Tanton, L.T., Burgess, S., and Yin, Q.-Z. (2011) The lunar magma ocean: Reconciling the solidification process with lunar petrology and geochronology, Earth and Planetary Science Letters, 304, 326-336.

Hapke, B. (1981) Bidirectional reflectance spectroscopy: 1. Theory, Journal of Geophysical Research – Solid Earth, 86, 3039–3054.

Hapke, B. (1993) Theory of Reflectance and Emittance Spectroscopy, 455 pp., Cambridge Univ. Press, New York.

Hapke, B. (2001) Space weathering from Mercury to the asteroid belt, J. Geophys. Res, 106, 10039-10073.

Hapke, B. (2002) Bidirectional reflectance spectroscopy, 5: The coherent backscatter opposition effect and anisotropic scattering, Icarus, 157, 532-534, doi:10.1006/icar.2002.6853.

Hazen, R.M., Mao, H.K., and Bell, P.M. (1977) Effects of compositional variation on absorption spectra of lunar olivines, Proceedings of the 8th Lunar and Planetary Science Conference, 1081–1090.

Hazen, R.M., Bell, P.M., and Mao, H.K. (1978) Effects of compositional variation on absorption spectra of lunar pyroxenes, Proceedings of the 9th Lunar and Planetary Science Conference, 2919-2934.

Heiken, G.H., McKay, D.S., and Fruland, R.M. (1973), Proceedings of the 4th Lunar and Planetary Science Conference, 251-265.

Herbert, F., Drake, M.J., Sonett, C.P., and Wiskerchen, M.J. (1977) Some thermal constraints on the thermal history of the lunar magma ocean, Proceedings of the 8th Lunar and Planetary Science Conference, 573-582.

Isaacson, P.J., and Pieters, C.M. (2010) Deconvolution of lunar olivine reflectance spectra: Implications for remote compositional assessment, Icarus, 210, 8-13.

Isaacson, P.J., Basu Sarbadhikari, A., Pieters, C.M., Klima, R.L., Hiroi, T., Liu, Y., and Taylor, L.A. (2011) The lunar rock and mineral characterization consortium: Deconstruction and integrated mineralogical, petrologic, and spectroscopic analyses of mare basalts, Meteoritics and Planetary Science, 46, 228-251, doi: 10.1111/j.1945-5100.2010.01148.x.

Jackson, C.R.M., Cheek, L.C., Parman, S.W., Cooper, R.F., and Pieters, C.M. (2012) Compositional constraints on lunar spinel anorthosite: Synthesis of spinel with variable iron content. Lunar and Planetary Science Conference, 43rd, Abstract 2335.

Jackson, C., Cheek, L., Williams, K., Donaldson Hanna, K., Pieters, C., Parman, S., Cooper, R., Dyar, D., Nelms, M., Salvatore, M., in review, Visible-infrared spectral properties of iron-bearing aluminate spinel under reduced conditions.

James, O.B. (1980) Rocks of the early lunar crust, Proceedings of the 11th Lunar and Planetary Science Conference, 365-393.

James, O.B., Lindstrom, M.M., and Flohr, M.K. (1989) Ferroan anorthosite from lunar breccia 64435: Implications for the origin and history of lunar ferroan anorthosites, Proceedings of the 19th Lunar and Planetary Science Conference, 219-243.

Johnson, J.R., and Hörz, F. (2003) Visible/near-infrared spectra of experimentally shocked plagioclase feldspars, Journal of Geophysical Research - Planets, 108, E11, 5120, doi:10.1029/2003JE002127.

Johnson, P.E., Smith, M.O., Taylor-George, S., and Adams, J.B. (1983) A semiempirical method for analysis of the reflectance spectra of binary mineral mixtures, Journal of Geophysical Research – Solid Earth, 88, 3557–3561.

King, T.V.V., and Ridley, W.I. (1987) Relation of the spectroscopic reflectance of olivine to mineral chemistry and some remote sensing implications, Journal of Geophysical Research – Solid Earth, 92, 11457-11469.

Klima, R.L., Pieters, C.M., and Dyar, M.D. (2007) Spectroscopy of synthetic Mg-Fe pyroxenes I: Spin-allowed and spin-forbidden crystal field bands in the visible and near-infrared, Meteoritics and Planetary Science, 42, 235-253, doi:10.1111/j.1945- 5100.2007.tb00230.x.

Klima, R.L., Pieters, C.M., and Dyar, M.D. (2008) Characterization of the 1.2 um M1 pyroxene band: Extracting cooling history from near-IR spectra of pyroxenes and pyroxene-dominated rocks, Meteoritics and Planetary Science, 43, 1591-1604, doi: 10.1111/j.1945-5100.2008.tb00631.x

Klima, R.L., Dyar, M.D., and Pieters, C.M. (2011) Near-infrared spectra of clinopyroxenes: Effects of calcium content and crystal structure, Meteoritics and Planetary Science, 46, 379-395, doi: 10.1111/j.1945-5100.2010.01158.x.

McCord, T.B., Clark, R.N., Hawke, B.R., McFadden, L.A., Owensby, P.D., Pieters, C.M., and Adams, J.B. (1981) Moon: Near-infrared spectral reflectance, A first good look, Journal of Geophysical Research – Solid Earth, 86, 10883–10892.

McGee, J.J. (1993) Lunar ferroan anorthosites: Mineralogy, compositional variations, and petrogenesis, Journal of Geophysical Research - Planets, 98, 9089-9105.

McKay, D.S., Heiken, G.S., Taylor, R.M., Clanton, U.S., Morrison, D.A., and Ladle, G.H. (1972), Proceedings of the 3rd Lunar and Planetary Science Conference, 983-994.

McKay, D.S., Fruland, R.M., and Heiken, G.H. (1974) Grain size evolution of lunar soils, Proceedings of the 5th Lunar and Planetary Science Conference, 887-906.

Mustard, J.F., and Pieters, C.M. (1987) Quantitative abundance estimates from bidirectional reflectance measurements, Journal of Geophysical Research – Solid Earth , 92, E617–E626.

Mustard, J.F., and Pieters, C.M. (1989) Photometric phase functions of common geologic minerals and applications to quantitative analysis of mineral mixture reflectance spectra, Journal of Geophysical Research – Solid Earth, 94, 13619–13634.

Nash, D.B., and Conel, J.E. (1974) Spectral reflectance systematics for mixtures of powdered hypersthene, labradorite, and ilmenite, Journal of Geophysical Research, 79, 1615-1621.

Noble, S.K., Pieters, C.M., and Keller, L.P. (2007) An experimental approach to understanding the optical effects of space weathering, Icarus, 192, 629-642, doi: 10.1016/j.icarus.2007.07.021.

Ohtake, M., Matsunaga, M.T., Haruyama, J., Yokota, Y., Morota, T., Honda, C., Ogawa, Y., Torii, M., Miyamoto, H., Arai, T., Hirata, N., Iwasaki, A., Nakamura, R., Hiroi, T., Sugihara, T., Takeda, H., Otake, H., Pieters, C.M., Saiki, K., Kitazato, K., Abe, M., Asada, N., Demura, H., Yamaguchi, Y., Sasaki, S., Kodama, S., Terazono, J., Shirao, M., Yamaji, A., Minami, S., Akiyama, H., and Josset, J. –L. (2009) The global distribution of pure anorthosite on the Moon, Nature, 461, 236-240, doi:10.1038/nature08317.

Pieters, C.M. (1982) Copernicus crater central peak: Lunar mountain of unique composition, Science, 215, 59-61.

Pieters, C. M. (1983) Strength of mineral absorption features in the transmitted component of near-infrared reflected light: First results from RELAB, Journal of Geophysical Research – Solid Earth, 88, 9534-9544, doi:10.1029/JB088iB11p09534.

Pieters, C. M., Taylor, L.A., Noble, S.K., Keller, L.P., Hapke, B., Morris, R.V., Allen, C.C., McKay, D.S., and Wentworth, S. (2000) Space weathering airless bodies: Resolving a mystery with lunar samples, Meteoritics and Planetary Science, 35, 1101-1107, doi:10.1111/j.1945-5100.2000.tb01496.x.

Pieters, C.M., Besse, S., Boardman, J., Buratti, B., Cheek, L., Clark, R.N., Combe, J.P., Dhingra, D., Goswami, J.N., Green, R.O., Head, J.W., Isaacson, P., Klima, R., Kramer, G., Lundeen, S., Malaret, E., McCord, T., Mustard, J., Nettles, J., Petro, N., Runyon, C., Staid, M., Sunshine, J., Taylor, L.A., Thaisen, K., Tompkins, S., and Whitten, J. (2011) Mg-spinel lithology: A new rock type on the lunar farside, *Journal of Geophysical Research - Planets*, *116*, E00G08.

Pieters, C.M., Donaldson, K.L., Cheek, L.C., Dhingra, D., Moriarty, D., Parman, S., Jackson, C., and Prissel, T.C. (2013) Compositional evolution of the early lunar crust: Observed diverse mineralogy of the upper and lower crust, *Lunar and Planetary Science Conference*, *44th*, Abstract 2545.

Pieters, C.M., Donaldson Hanna, K.L., Cheek, L., Dhingra, D., Prissel, T.C., Jackson, C.R.M., Moriarty, D.P., Parman, S.W., and Taylor, L.A., The distribution and origin of Mg-Spinel on the Moon, *in press.*

Ryder, G., and Norman, M. (1978), *Catalog of pristine non-mare materials, Part 2, Anorthosites*, 86 pp., Curator, NASA Johnson Space Center, Houston.

Serventi, G., Carli, C., Sgavetti, M., Ciarniello, M., Capaccioni, F., and Pedeazzi, G. (2013a) Spectral variability of plagioclase-mafic mixtures (1): Effects of chemistry and modal abundance in reflectance spectra of rocks and mineral mixtures, *Icarus, 226*, 282-298.

Serventi, G., Carli, C., and Sgavetti, M., (2013b) Plagioclase influence in mixtures with very low mafic mineral content., *Lunar and Planetary Science Conference*, *44th*, Abstract 1490.

Singer, R. B. (1981) Near-infrared spectral reflectance of mineral mixtures: Systematic combinations of pyroxenes, olivine, and iron oxides, *Journal of Geophysical Research – Solid Earth*, *86*, 7967–7982.

Smith, J.V., Anderson, A.T., Newton, R.C., Olsen, E.J., Wyllie, P.J., Crewe, A.V., Isaacson, M.S., and Johnson, D. (1970) Petrologic history of the moon inferred from petrography, mineralogy, and petrogenesis of Apollo 11 rocks, *Proceedings of the Apollo 11 Lunar Science Conference,* 897-925.

Spudis, P.D., Hawke, B.R., and Lucey, P. (1984) Composition of Orientale basin deposits and implications for the lunar basin-forming process, *Proceedings of the 15th Lunar and Planetary Science Conference Sci., Part 1*, C197-C210.

Stöffler, D. (1971) Progressive metamorphism and classification of shocked and brecciated crystalline rocks at impact craters, *Journal of Geophysical Research, 76*, 5541-5551.

Stöffler, D., Knoell, H. –D., Marvin, U.B., Simonds, C.H., and Warren, P.H. (1980) Recommended classification and nomenclature of lunar highland rocks- A committee report, in *Proceedings of the Conference on the Lunar Highland Crust*, edited by J. J. Papike, and R. B. Merrill, p. 51-70, Pergamon Press, New York.

Suckale, J., Elkins-Tanton, L.T., and Sethian, J.A. (2012) Crystals stirred up: 2. Numerical insights into the formation of the earliest crust on the Moon, *Journal of Geophysical Research - Planets, 117*, E08005, doi:10.1029/2012JE004067.

Sunshine, J.M., and Pieters, C.M. (1998) Determining the composition of olivine from reflectance spectroscopy, *Journal of Geophysical Research - Planets*, 103, 13675-13688.

von Engelhardt, W., and Stöffler, D. (1968) Stages of shock metamorphism in crystalline rocks of the Ries Basin, Germany, in *Shock Metamorphism of Natural Materials*, edited by B. M. French and N. M. Short, p.159-168, Mono Book Corp., Baltimore, M. D.

Warren, P.H., and Wasson, J.T. (1977) Pristine nonmare rocks and the nature of the lunar crust, *Proceedings of the 8th Lunar and Planetary Science Conference,* 2215-2235.

Warren, P.H., and Wasson, J.T. (1980) Early lunar petrogenesis, oceanic and extraoceanic, in *Proceedings of the Conference on the Lunar Highland Crust*, edited by J. J. Papike, and R. B. Merrill, p. 81-99, Pergamon Press, New York.

Warren, P.H. (1990) Lunar anorthosites and the magma-ocean plagioclase-flotation hypothesis: Importance of FeO enrichment in the parent magma, *American Mineralogist, 75*, 46-58.

Wood, J.A., Dickey, J.S. Jr., Marvin, U.B., and Powell, B.N. (1970) Lunar anorthosites and a geophysical model of the moon, *Proceedings of the Apollo 11 Lunar Science Conference*, 965-988.

Yamamoto, S., Nakamura, R., Matsunaga, T., Ogawa, Y., Ishihara, Y., Morota, T., Hirata, N., Ohtake, M., Hiroi, T., Yokota, Y., and Hauyama, J. (2010) Possible mantle origin of olivine around lunar impact basins detected by SELENE, *Nature Geoscience, 3*, 533-536.

Yamamoto, S., Nakamura, R., Matsunaga, T., Ogawa, Y., Ishihara, Y., Morota, T., Hirata, N., Ohtake, M., Hiroi, T., Yokota, Y., and Haruyama, J. (2012) Massive layer of pure anorthosite on the Moon*, Geophysical Research Letters, 39*, L13201, doi:10.1029/2012GL052098.

Yamamoto, S., Nakamura, R., Matsunaga, T., Ogawa, Y., Ishihara, Y., Morota, T., Hirata, N., Ohtake, M., Hiroi, T., Yokota, Y., and Haruyama, J., A new type of pyroclastic deposit on the Moon containing Fe-spinel and chromite, *Geophysical Research Letters*, *40*, 4549 – 4554, doi: 10.1002/grl.50784.

FIGURE CAPTIONS

Figure 1. Near-infrared reflectance spectra of common lunar minerals measured in RELAB. All are 0-125 µm separates from Apollo samples (Isaacson et al., 2011), with the exception of the spinel, which is a terrestrial sample consisting of 1-2 mm crystals. (a) Plagioclase separate from highland soil 62240 (RELAB: LR-CMP-183). (b) Olivine separate from low-Ti basalt 15555 (RELAB: LR-CMP-169). The weak absorption near 2000 nm is likely due to chromite inclusions. (c) Orthopyroxene separate from low-Ti basalt 15058 (RELAB: LR-CMP-173). (d) Clinopyroxene separate from high-Ti basalt 70017 (RELAB: LR-CMP-175) The broad absorption short of 800 nm in this sample is likely due to particularly high titanium content, and is not considered diagnostic of typical high-calcium pyroxene. (e) Gem quality pink spinel from Sri Lanka (RELAB: SP-SWP-028).

Figure 2. Example Moon Mineralogy Mapper (M^3) spectra from Copernicus, Tsiolkovskiy, and Orientale displaying a range of spectral characteristics that suggest mixing of plagioclase with variable proportions of mafic minerals. The bar spanning 1000-1500 nm annotates the spectral region of interest for combination of plagioclase and mafic mineral absorption features. (a) Spectra resembling pure plagioclase. We interpret the Tsiolkovskiy spectrum in (a) as representing plagioclase plus very small amounts of either olivine or pyroxene causing the absorption to broaden. (b) Spectra displaying composite absorptions likely implying minor mafic components within an anorthositic bulk lithology. (c) Spectra dominated by a mafic component. Continuum-removed versions of a-c are shown in d-f, respectively. The continuum for each spectrum was calculated as a straight line between tie points defined by the reflectance maximum between 540 and 900 nm (short-wavelength tie-point) and between 1350 and 1900 nm (long-wavelength tie-point).

Figure 3. The terrestrial plagioclase endmember used in the laboratory mixing analyses (top spectrum, solid line). Shown for comparison are a plagioclase separate from a lunar highland soil (dotted line) and lunar anorthosite 60025 (dashed line). The terrestrial endmember and the lunar anorthosite both consist of 45-75 µm particles. The highland soil plagioclase has a particle size of 0-125 µm (RELAB ID: LR-CMP-183). The terrestrial sample was wet-sieved with de-ionized water to remove adhering fine particles.

Figure 4. Average Mg number in olivine and opx versus An number in plagioclase for pristine lunar nonmare rocks (digitized from Warren and Wasson, 1979; open and filled circles). The Mg numbers of the olivine and orthopyroxene terrestrial samples used as endmembers in this study are overplotted as horizontal lines. Two distinct compositional groups are identified in the lunar data: the Mg-suite materials (open circles) and the ferroan anorthosites (filled circles), which are overall much less magnesian. The two olivine and one orthopyroxene endmembers used in this study generally bracket the mafic compositions that occur in the pristine lunar nonmare samples.

Always consult and cite the final, published document. See http://www.minsocam.org or GeoscienceWorld

Figure 5. Mafic mineral endmembers used in the laboratory mixing analysis. All samples were wet-sieved with de-ionized water to 45-75 µm. (a) The two olivine endmembers: $Olv1_{Fo91}$ from San Carlos, AZ (top spectrum), and $Olv1_{Fo47,}$ separated from a sample from the Kiglapait intrusion (bottom spectrum). (b) The two pyroxene endmembers: an orthopyroxene (enstatite) from Bamble, Norway, and a diopside from Madagascar. (c) The two spinel endmembers: a very high Mg spinel (Mg98) from Tanzania (top spectrum), and an Mg-spinel (Mg87) from Amity, NY (bottom spectrum).

Figure 6. Sequence of mineral mixing procedures, using as an example the mature soil particle size distribution. In step 1, each of the mineral endmembers are divided into three broad particle size separates: <45 µm, 45-250 µm, and 250-1000 µm. In step 2, these three particle size fractions are combined in specific proportions by mass to create a distribution. In this case, the <45 µm, 45-250 µm, and 250-1000 µm splits go to represent 50%, 30%, and 20% by mass, respectively (for the immature distribution, they are combined as 20%, 30%, 50%, respectively). In step 3, binary mixtures of 93 vol% plagioclase and 7 vol% non-plagioclase endmembers, each containing a wide particle size distribution, are combined.

Figure 7. All six binary mixture series with particle sizes 45-75 µm produced for this study. (a) Plagioclase plus variable amounts of $Olv1_{Fo91}$. The legend and color scheme are the same in subsequent parts of the figure, (b) Plagioclase plus $Olv1_{Fo47}$, (c) plagioclase plus Opx_{Mg88}, (d) plagioclase plus $Diop_{En46}$, (e) plagioclase plus the $Sp1_{Mg98}$ endmember, (f) plagioclase plus the Mg-Spinel endmember.

Figure 8. Mixture series (45-75 µm particles) displayed according to the volume percent of olivine, pyroxene, or spinel in each mixture. Only the mixtures that are strictly analogous to anorthosites, containing ≥90 vol% plagioclase, are shown (a) The six binary mixtures containing plagioclase plus 2 vol% non-plagioclase minerals. The spectra are labeled in part a only, but their order and color is maintained throughout all parts of the figure. (b) Mixtures containing plagioclase plus 5 vol% non-plagioclase minerals, (c) mixtures containing plagioclase plus 7 vol% non-plagioclase minerals, (d) plagioclase plus 10 vol% non-plagioclase minerals, (e) plagioclase plus 15 vol% non-plagioclase minerals, (f) plagioclase plus 25 vol% non-plagioclase minerals.

Figure 9. Laboratory prepared mixtures containing 15 (a-c), 25 (d-f), or 50 (g-i) vol% olivine, pyroxene, or spinel (45-75 µm particles). The corresponding mineral endmembers are plotted as dashed lines, the mixtures are plotted as solid lines. The endmember and mixture spectra have been scaled near the reflectance maximum below 1000 nm, and each pair of spectra was vertically offset for clarity. (a) 15 vol% olivine, (b) 15 vol% pyroxene, (c) 15 vol% spinel, (d) 25 vol% olivine, (e) 25 vol% pyroxene, (f) 25 vol% spinel, (g) 50 vol% olivine, (h) 50 vol% pyroxene, (i) 50 vol% spinel.

Figure 10. Schematic of the parameter for estimating relative band depths of the plagioclase and mafic components in a given spectrum, shown for two of the mixtures containing Olv1$_{Fo91}$. A negative slope for the 2 vol% olivine mixture corresponds to a relatively strong plagioclase component. A positive slope for the 10 vol% olivine mixture indicates a more dominant mafic component

Figure 11. Slope parameter estimating relative plagioclase-mafic absorption depths. Higher slope values correspond to a relatively stronger mafic absorption. (a) Slope parameter values shown for all mixtures in the four mafic silicate series. (b) Slope parameter values shown for only the mixtures containing ≤10 vol% mafics.

Figure 12. Two different soil size distributions compared with the constrained 45-75 μm size fraction for mixtures containing 7% olivine, pyroxene, or spinel. No continuum has been removed. (a) 7% Olv1$_{Fo91}$, (b) 7% Opx$_{Mg88}$, (c) 7% Sp1$_{Mg98}$, (d) 7% Olv1$_{Fo91}$, scaled to the reflectance maximum between 650 and 800 nm, (e) 7% Opx$_{Mg88}$, scaled as in (d), (f) 7 vol% Sp1$_{Mg98}$, scaled as in (d).

Figure 13. All six laboratory prepared mixture series (solid lines), the same as in Figure 7, plotted with the best fit modeled mixtures calculated using the inverse Hapke modeling approach (dotted lines).

Figure 14. The non-plagioclase abundance (vol% solids) of the best-fit modeled spectrum plotted against the abundances prepared in the laboratory.

Figure 15. Proportion of mafic minerals in each best-fit modeled spectrum compared with the proportion of mafics in the corresponding laboratory prepared mixture. More positive slope values correspond to a higher mafic mineral abundance. A slope of zero corresponds to equal plagioclase and mafic absorption band depths, and negative values indicate that the plagioclase absorption is deeper than the mafic absorption in the continuum-removed spectrum. (a) Comparison of measured vs. modeled absorption depths for all mixtures. (b) Comparison of measured vs. modeled absorption depths for only the mixtures containing mafic abundances ≤10 vol%.

Figure 16. All six laboratory mixture series (solid lines), the same as in Figure 6, plotted with modeled mixtures calculated using the forward modeling approach (dotted lines).

Figure 17. Endmember synthetic orthopyroxenes used in a forward model to characterize the effect of pyroxene composition on the spectra of plagioclase-dominated mixtures. These samples are from the suite studied by Klima et al. (2007), and were specifically chosen to span a wide

range of En numbers. En90: RELAB ID: DL-CMP-065. En70: RELAB ID DL-CMP-026. En50: RELAB ID DL-CMP-004. En30: RELAB ID DL-CMP-023.

Figure 18. Model plagioclase – orthopyroxene mixtures produced using the Hapke forward model, with four synthetic orthopyroxene spectra as the mafic endmember (Klima et al. 2007). (a) 2 vol% orthopyroxene, (b) 5 vol% orthopyroxene, (c) 7 vol% orthopyroxene, (d) 10 vol% orthopyroxene.

Figure A1. Residual Spectra (measured – best fit modeled spectra in reflectance) for the Plagioclase + $Olv1_{Fo91}$ series. The measured spectra were prepared in the laboratory with a particle size range of 45-75 µm. The modeled spectra were calculated using the inverse Hapke model with best fit proportions constrained to be positive and normalized to one.

Figure A2. Residual Spectra (measured – best fit modeled spectra in reflectance) for the Plagioclase + $Olv2_{Fo47}$ series. The measured spectra were prepared in the laboratory with a particle size range of 45-75 µm. The modeled spectra were calculated using the inverse Hapke model with best fit proportions constrained to be positive and normalized to one.

Figure A3. Residual Spectra (measured – best fit modeled spectra in reflectance) for the Plagioclase + Opx_{Mg88} series. The measured spectra were prepared in the laboratory with a particle size range of 45-75 µm. The modeled spectra were calculated using the inverse Hapke model with best fit proportions constrained to be positive and normalized to one.

Figure A4. Residual Spectra (measured – best fit modeled spectra in reflectance) for the Plagioclase + $Diop_{En46}$ series. The measured spectra were prepared in the laboratory with a particle size range of 45-75 µm. The modeled spectra were calculated using the inverse Hapke model with best fit proportions constrained to be positive and normalized to one.

Figure A5. Residual Spectra (measured – best fit modeled spectra in reflectance) for the Plagioclase + $Sp1_{Mg98}$ series. The measured spectra were prepared in the laboratory with a particle size range of 45-75 µm. The modeled spectra were calculated using the inverse Hapke model with best fit proportions constrained to be positive and normalized to one.

Figure A6. Residual Spectra (measured – best fit modeled spectra in reflectance) for the Plagioclase + $Sp2_{Mg87}$ series. The measured spectra were prepared in the laboratory with a particle size range of 45-75 µm. The modeled spectra were calculated using the inverse Hapke model with best fit proportions constrained to be positive and normalized to one.

Table 1. Endmember samples and brief descriptions of processing

Sample name	Mineral type	Description of sample and processing
Plagioclase	Plagioclase	Yellow Labradorite from Mexico. Seven 2-3 cm transparent, inclusion-free stones were crushed together to create a homogeneous sample.
$Olv1_{Fo91}$	Olivine (magnesian)	San Carlos olivine that consisted of four ~1 cm grains with very minor inclusions of spinel or chromite that were removed by handpicking.
$Olv2_{Fo47}$	Olivine (intermediate)	Kiglapait olivines were obtained from a cut slab of a bulk rock sample, which also contained abundant plagioclase and some pyroxene. Most of the olivine was separated by crushing the bulk sample and passing the particulate material (principally 125-500 µm) through a magnetic separator. The olivine split was further crushed and again passed through a magnetic separator in order to remove most inclusions (likely spinel).
Opx_{Mg88}	Orthopyroxene	Enstatite from Bamble, Norway that was obtained from Ward's Science. Most grains are tan or grey in color. Inspection under a binocular microscope indicates the presence of a minor fibrous component, suggested to be tremolite by *Singer* [1981]. The orthopyroxene was previously separated from a bulk rock by David Crown [*Crown and Pieters*, 1987].
$Diop_{En46}$	Diopside	The diopside endmember is from Madagascar and was obtained from Ward's Science. Most grains are green in color. The grains with the least amount of oxidation and impurities were selected for the analysis. These were crushed and additional impurities were removed by hand-picking.
$Sp1_{Mg98}$	Mg-Spinel (very high Mg)	Six transparent inclusion-free crystals from Tanzania. Each crystal was 1-2 cm in size and displayed a deep purple color.
$Sp2_{Mg87}$	Mg-Spinel (high Mg)	1-2 cm black spinel crystals (many euhedral) from Amity, New York that were separated from a calcite-dominated rock manually. Adhering calcite was removed by dissolving in 6N HCl for 12-48 hours.

Always consult and cite the final, published document. See http://www.minsocam.org or GeoscienceWorld

Table 2. Endmember major element compositions (wt%)[a]

	Plagioclase	**Olv1$_{Fo91}$**	**Olv2$_{Fo47}$**	**Opx$_{Mg88}$**	**Diop$_{En46}$**	**Sp1$_{Mg98}$**	**Sp2$_{Mg87}$**
Mineral	Plagioclase	Olivine	Olivine	Orthopyroxene	Diopside	Mg-Spinel	Mg-Spinel
Source	Mexico	San Carlos	Kiglapait	Norway	Madagascar	Tanzania	New York
n	*123*	*40*	*40*	*54*	*40*	*60*	*10*
Na_2O	4.48	0.01	0.00	0.01	0.16	n/a	n/a
MgO	0.11	49.98	21.48	33.96	16.15	27.48	23.49
Al_2O_3	29.98	0.02	0.00	0.15	4.42	70.36	69.51
SiO_2	52.81	41.06	34.22	57.43	51.42	0.02	0.03
K_2O	0.28	0.00	0.00	0.00	0.00	n/a	n/a
CaO	12.06	0.08	0.06	0.29	24.64	0.00	0.00
TiO_2	0.07	0.00	0.01	0.06	0.28	0.00	0.03
Cr_2O_3	n/a	0.02	0.00	0.01	0.00	0.10	0.07
MnO	n/a	0.13	0.57	0.05	0.07	0.03	0.13
FeO	0.35	9.01	43.59	7.90	2.64	1.10	6.02
NiO	n/a	0.38	0.01	0.02	0.00	0.00	0.01
ZnO	n/a	n/a	n/a	n/a	n/a	0.78	1.05
Total	100.14	100.69	99.94	99.88	99.78	99.87	100.34
An#[b]	58.88	n/a	n/a	n/a	n/a	n/a	n/a
Mg#[c]	n/a	90.82	46.76	88.45	91.59	97.80	87.43
En#[d]	n/a	n/a	n/a	87.97	45.70	n/a	n/a
Fs#	n/a	n/a	n/a	11.49	4.20	n/a	n/a
Wo#	n/a	n/a	n/a	0.54	50.10	n/a	n/a
Density (g/cm$^{\wedge 3}$)[e]	2.70	3.33	3.85	3.30	3.34	3.57	3.64

[a] All mineral compositions analyzed using a Cameca SX100 electron microprobe at Brown University.

[b]An = molar (Ca/(Ca+Na+K)); [c]Mg= molar (Mg/(Mg+Fe)); [d]En = molar (Mg/(Mg+Fe+Ca)); [e]Fs = molar (Fs/(Mg+Fe+Ca)); [f]Wo = molar (Ca/(Mg+Fe+Ca)); [g] Density values were calculated for each endmember from the mass and volume of the unit cell based on the cell parameters given in *Deer et al.*, (1992).

Always consult and cite the final, published document. See http://www.minsocam.org or GeoscienceWorld

Table 3. Measured (laboratory prepared) and Modeled (best fit) abundances

Nominal Vol% Plag		Measured Mass%		Measured Vol % [a]		Modeled Best Fit Mass%		Modeled Best Fit Vol% (weighting factor) [b]		Measured - Best Fit Vol% Mafic	Best Fit RMSE
Plag	Olv1$_{Fo91}$										
98	2	97.5	2.5	98.0	2.0	96.2	3.8	96.9	3.1	-1.1	5.24E-03
95	5	93.9	6.1	95.0	5.0	92.1	7.9	93.5	6.5	-1.5	3.40E-03
93	7	91.5	8.5	93.0	7.0	89.3	10.7	91.1	8.8	-1.9	3.28E-03
90	10	87.9	12.1	90.0	10.0	87.4	12.6	89.5	10.5	-0.4	3.67E-03
85	15	82.2	17.8	85.1	14.9	78.0	22.0	81.4	18.6	-3.7	6.22E-03
75	25	70.9	29.1	75.0	25.0	67.9	32.1	72.3	27.7	-2.7	4.60E-03
50	50	46.1	53.9	51.4	48.6	39.2	60.8	44.3	55.7	-7.0	2.39E-03
Plag	Olv2$_{Fo47}$										
98	2	97.2	2.8	98.0	2.0	97.1	2.9	98.0	2.0	0.0	4.98E-03
95	5	93.0	7.0	95.0	5.0	92.4	7.6	94.5	5.5	-0.5	3.45E-03
93	7	90.3	9.7	93.0	7.0	89.1	10.9	92.1	7.9	-0.9	5.41E-03
90	10	86.3	13.7	90.0	10.0	84.3	15.7	88.4	11.6	-1.5	4.37E-03
85	15	79.8	20.2	85.0	15.0	73.5	26.5	79.8	20.1	-5.1	7.02E-03
75	25	67.9	32.1	75.1	24.9	62.1	37.9	69.8	30.0	-5.1	6.36E-03
50	50	41.1	58.9	49.8	50.2	35.4	64.6	43.9	56.1	-5.9	5.76E-03
Plag	Opx$_{Mg88}$										
98	2	97.5	2.5	97.9	2.1	97.6	2.4	98.0	2.0	0.1	2.21E-03
95	5	93.9	6.1	95.0	5.0	93.8	6.2	94.9	5.1	-0.1	3.31E-03
93	7	91.9	8.1	93.2	6.8	91.5	8.5	93.0	7.0	-0.3	6.88E-03
90	10	88.0	12.0	89.9	10.1	87.7	12.3	89.7	10.3	-0.2	2.65E-03
85	15	82.2	17.8	84.9	15.1	83.2	16.8	85.8	14.2	0.9	3.27E-03
75	25	71.1	28.9	75.1	24.9	73.1	26.9	76.9	23.1	1.9	4.17E-03
50	50	44.9	55.1	49.9	50.1	46.0	54.0	51.0	49.0	1.2	6.60E-03

Always consult and cite the final, published document. See http://www.minsocam.org or GeoscienceWorld

Plag	Diop$_{\text{En46}}$										
98	2	97.5	2.5	98.0	2.0	97.8	2.2	98.2	1.8	0.2	7.19E-03
95	5	93.8	6.2	94.9	5.1	92.9	7.1	94.2	5.8	-0.7	2.35E-03
93	7	91.5	8.5	93.0	7.0	90.2	9.8	91.9	8.1	-1.1	3.37E-03
90	10	88.0	12.0	90.0	10.0	86.1	13.9	88.4	11.6	-1.6	2.21E-03
85	15	82.0	18.0	85.0	15.0	78.7	21.3	82.1	17.9	-2.9	1.34E-02
75	25	70.9	29.1	75.1	24.9	63.9	36.1	68.7	31.4	-6.5	1.30E-02
50	50	44.8	55.2	50.1	49.9	38.0	62.0	43.1	56.9	-7.0	7.49E-03
Plag	Sp1$_{\text{Mg98}}$										
98	2	97.3	2.7	98.0	2.0	98.0	2.0	98.5	1.5	0.5	8.68E-03
95	5	93.5	6.5	95.0	5.0	93.0	7.0	94.6	5.4	-0.4	5.10E-03
93	7	90.9	9.1	93.0	7.0	90.4	9.6	92.6	7.4	-0.4	3.31E-03
90	10	87.1	12.9	89.9	10.1	86.6	13.4	89.6	10.4	-0.4	3.38E-03
85	15	81.0	19.0	85.0	15.0	79.2	20.8	83.4	16.5	-1.5	5.82E-03
75	25	69.4	30.6	75.0	25.0	65.3	34.7	71.3	28.7	-3.6	5.75E-03
50	50	43.1	56.9	50.0	50.0	36.5	63.5	43.1	56.8	-6.9	4.79E-03
Plag	Sp2$_{\text{Mg87}}$										
98	2	97.4	2.6	98.0	2.0	97.1	2.9	97.8	2.2	-0.2	9.86E-03
95	5	93.3	6.7	94.9	5.1	92.9	7.1	94.6	5.4	-0.3	1.03E-02
93	7	90.9	9.1	93.1	6.9	90.0	10.0	92.4	7.6	-0.7	9.58E-03
90	10	87.0	13.0	90.0	10.0	86.0	14.0	89.3	10.8	-0.8	9.51E-03
85	15	80.7	19.3	84.9	15.1	77.9	22.1	82.7	17.4	-2.3	1.45E-02
75	25	69.0	31.0	75.0	25.0	64.5	35.5	71.1	29.1	-4.1	1.68E-02
50	50	42.6	57.4	50.0	50.0	37.3	62.7	44.6	55.7	-5.6	1.23E-02

[a] Calculated from the mass of each component weighed out on a balance and the densities given in Table 2.

[b] Proportion of the mafic endmember that best fit the measured (laboratory prepared) mixture spectrum.

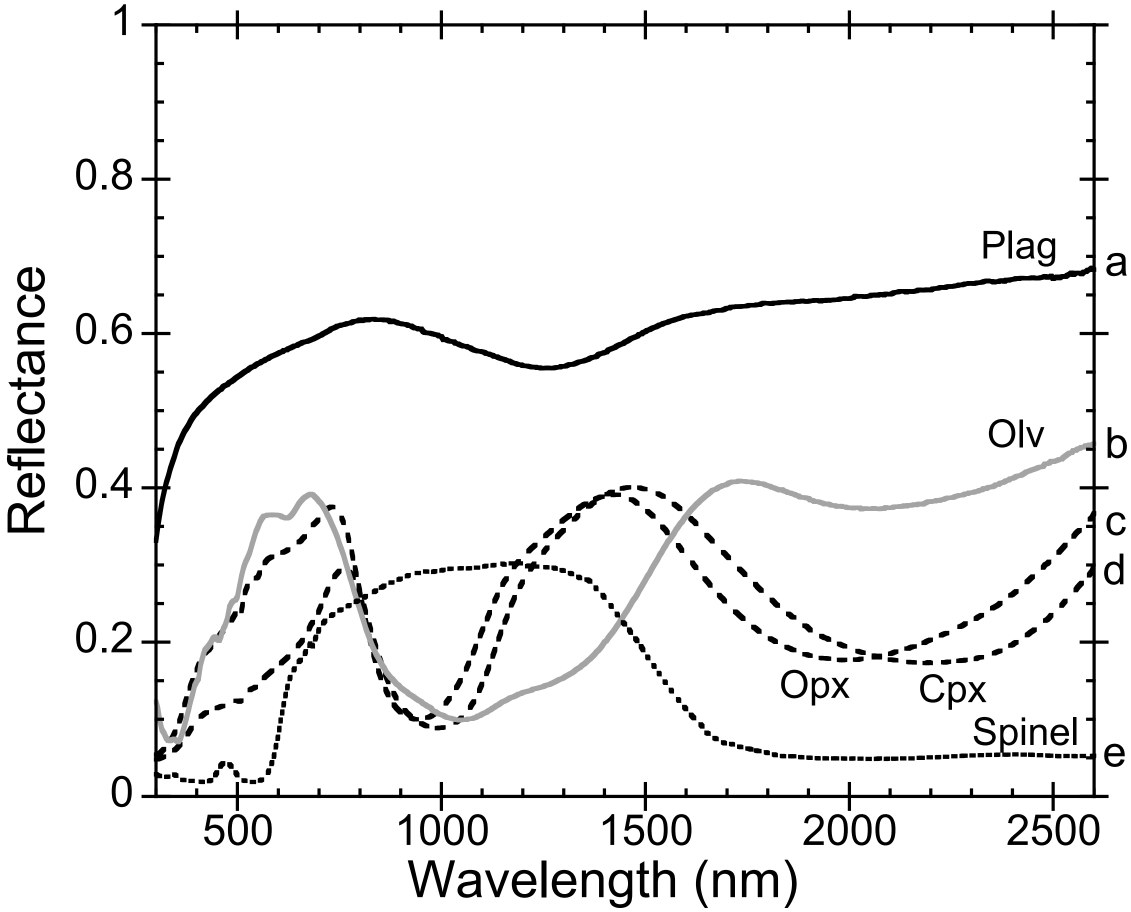

Figure 1. Near-infrared reflectance spectra of common lunar minerals measured in RELAB. All are 0-125 μm separates from Apollo samples (Isaacson et al., 2011), with the exception of the spinel, which is a terrestrial sample consisting of 1-2 mm crystals. (a) Plagioclase separate from highland soil 62240 (RELAB: LR-CMP-183). (b) Olivine separate from low-Ti basalt 15555 (RELAB: LR-CMP-169). The weak absorption near 2000 nm is likely due to chromite inclusions. (c) Orthopyroxene separate from low-Ti basalt 15058 (RELAB: LR-CMP-173). (d) Clinopyroxene separate from high-Ti basalt 70017 (RELAB: LR-CMP-175) The broad absorption short of 800 nm in this sample is likely due to particularly high titanium content, and is not considered diagnostic of typical high-calcium pyroxene. (e) Gem quality pink spinel from Sri Lanka (RELAB: SP-SWP-028).

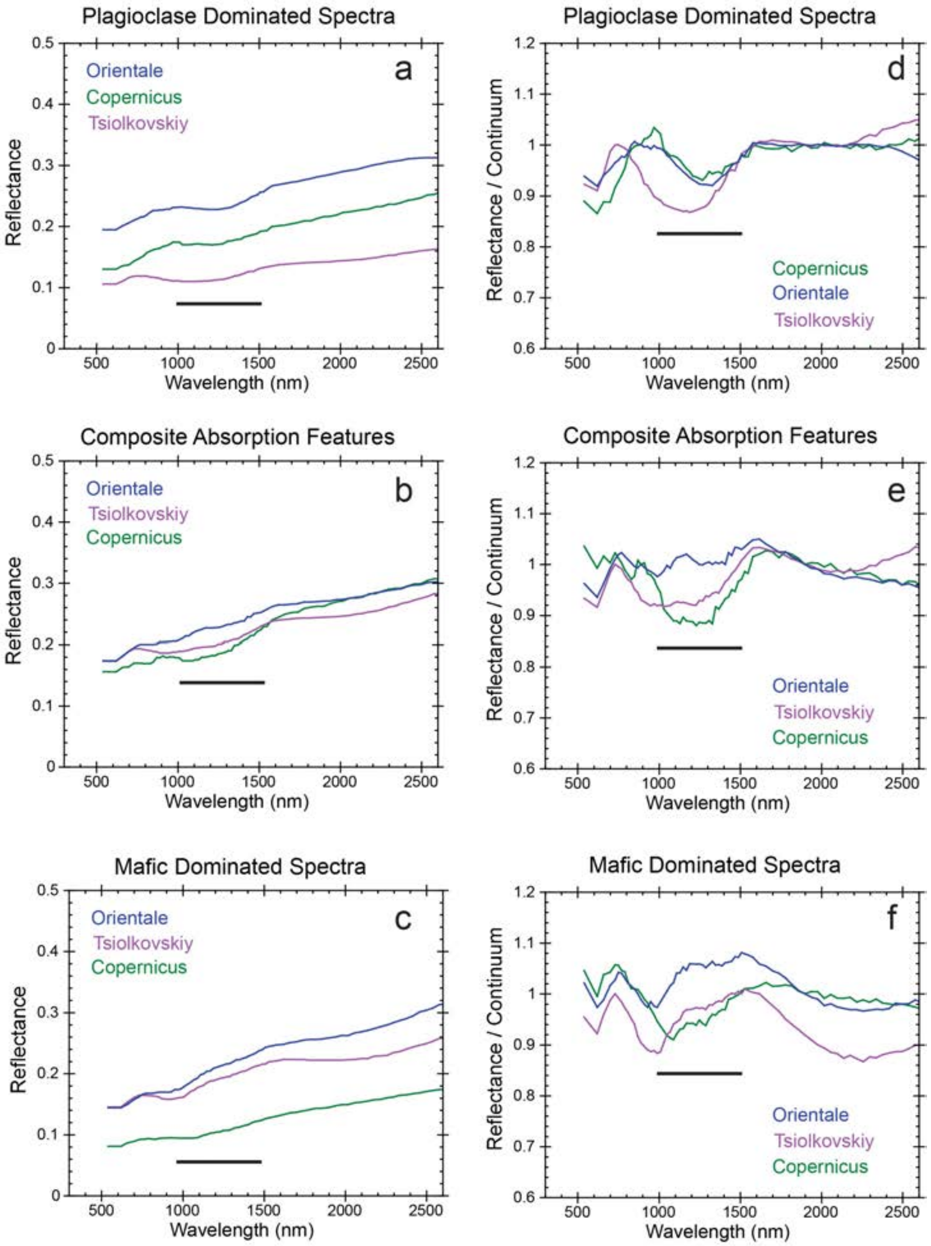

Figure 2. Example Moon Mineralogy Mapper (M^3) spectra from Copernicus, Tsiolkovskiy, and Orientale displaying a range of spectral characteristics that suggest mixing of plagioclase with variable proportions of mafic minerals. The bar spanning 1000-1500 nm annotates the spectral region of interest for combination of plagioclase and mafic mineral absorption features. (a) Spectra resembling pure plagioclase. We interpret the Tsiolkovskiy spectrum in (a) as representing plagioclase plus very small amounts of either olivine or pyroxene causing the absorption to broaden. (b) Spectra displaying composite absorptions likely implying minor mafic components within an anorthositic bulk lithology. (c) Spectra dominated by a mafic component. Continuum-removed versions of a-c are shown in d-f, respectively. The continuum for each spectrum was calculated as a straight line between tie points defined by the reflectance maximum between 540 and 900 nm (short-wavelength tie-point) and between 1350 and 1900 nm (long-wavelength tie-point).

This is a preprint, the final version is subject to change, of the American Mineralogist (MSA)
Cite as Authors (Year) Title. American Mineralogist, in press.
(DOI will not work until issue is live.) DOI: http://dx.doi.org/10.2138/am-2014-4785

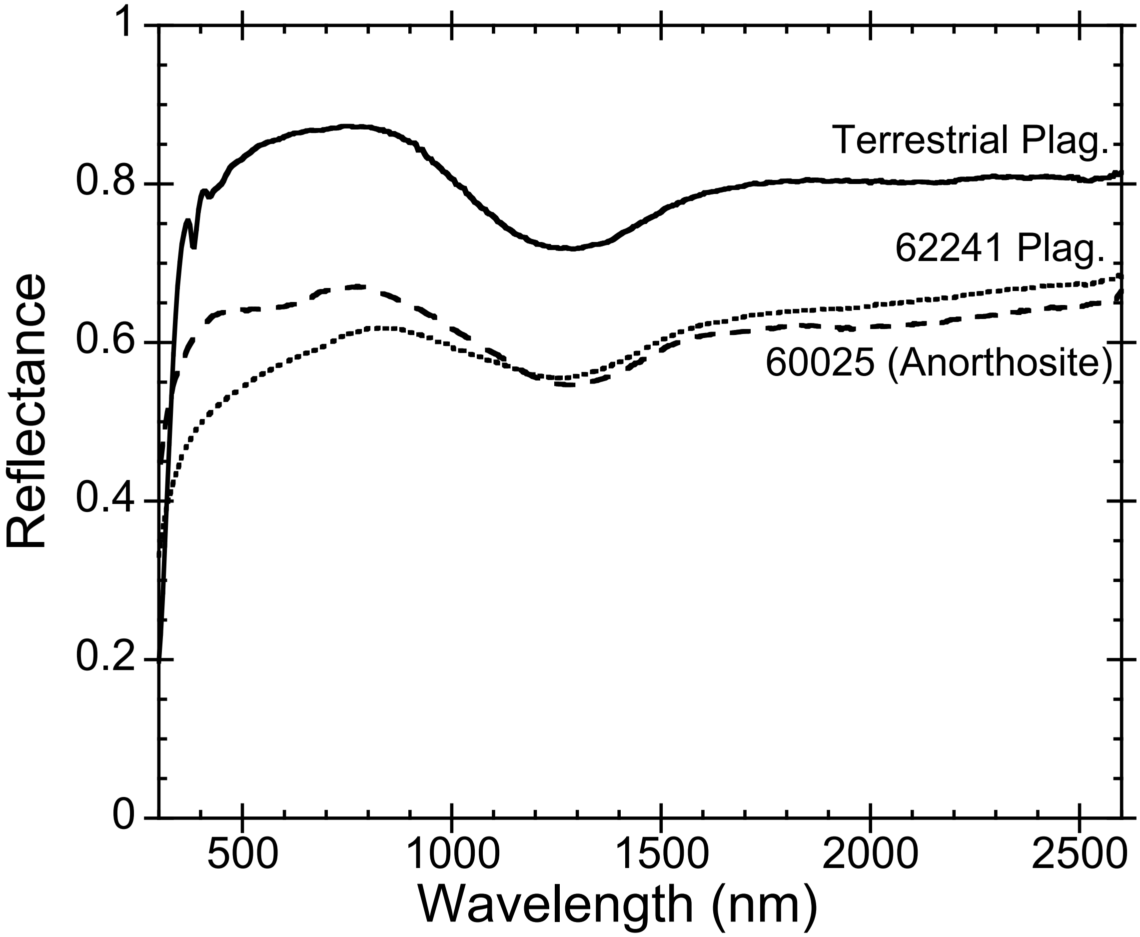

Figure 3. The terrestrial plagioclase endmember used in the laboratory mixing analyses (top spectrum, solid line). Shown for comparison are a plagioclase separate from a lunar highland soil (dotted line) and lunar anorthosite 60025 (dashed line). The terrestrial endmember and the lunar anorthosite both consist of 45-75 μm particles. The highland soil plagioclase has a particle size of 0-125 μm (RELAB ID: LR-CMP-183). The terrestrial sample was wet-sieved with de-ionized water to remove adhering fine particles.

Always consult and cite the final, published document. See http://www.minsocam.org or GeoscienceWorld

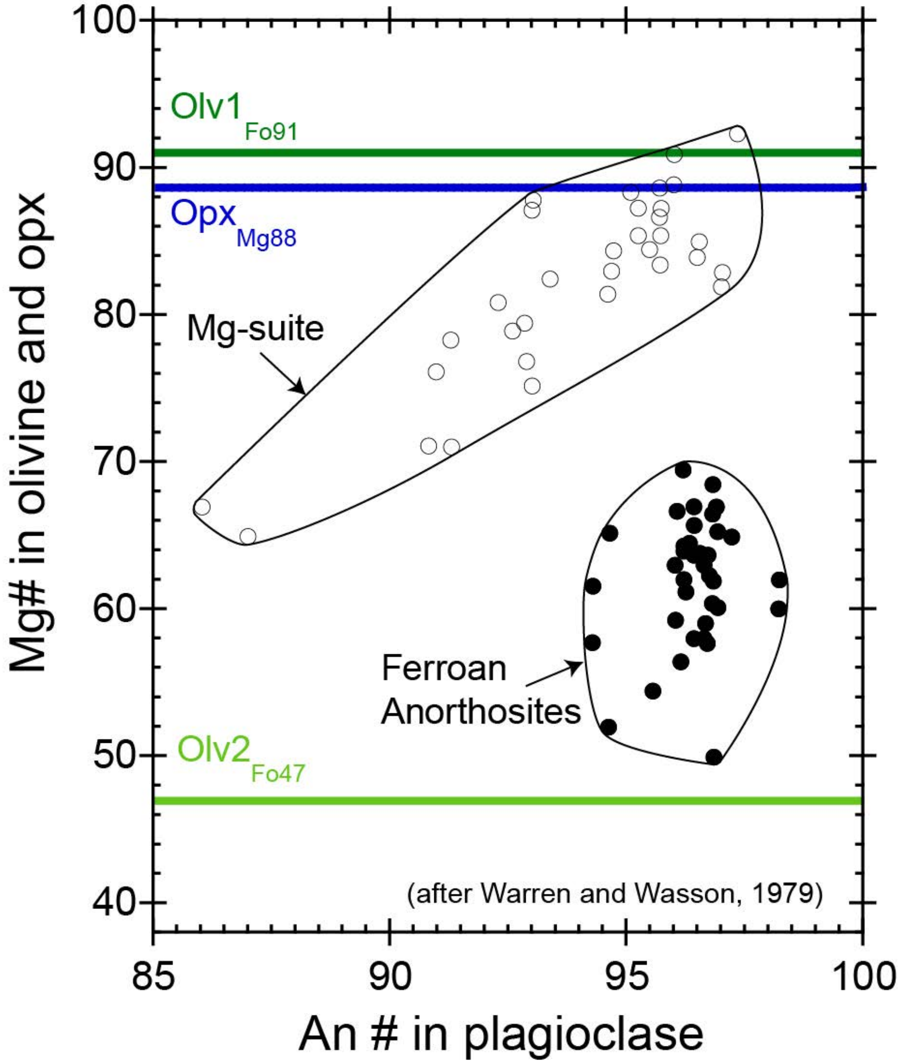

Figure 4. Average Mg number in olivine and opx versus An number in plagioclase for pristine lunar nonmare rocks (digitized from Warren and Wasson, 1979; open and filled circles). The Mg numbers of the olivine and orthopyroxene terrestrial samples used as endmembers in this study are overplotted as horizontal lines. Two distinct compositional groups are identified in the lunar data: the Mg-suite materials (open circles) and the ferroan anorthosites (filled circles), which are overall much less magnesian. The two olivine and one orthopyroxene endmembers used in this study generally bracket the mafic compositions that occur in the pristine lunar nonmare samples.

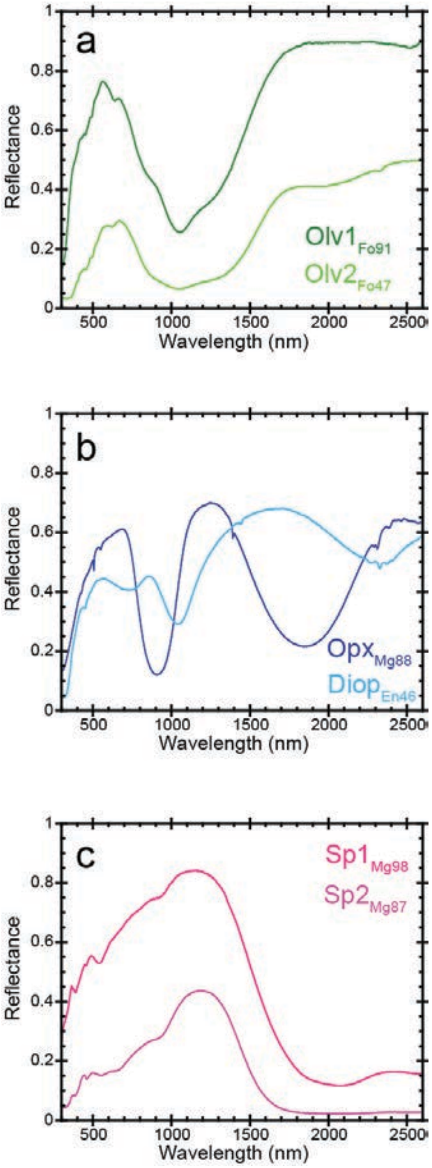

Figure 5. Mafic mineral endmembers used in the laboratory mixing analysis. All samples were wet-sieved with de-ionized water to 45-75 µm. (a) The two olivine endmembers: $Olv1_{Fo91}$ from San Carlos, AZ (top spectrum), and $Olv1_{Fo47,}$ separated from a sample from the Kiglapait intrusion (bottom spectrum). (b) The two pyroxene endmembers: an orthopyroxene (enstatite) from Bamble, Norway, and a diopside from Madagascar. (c) The two spinel endmembers: a very high Mg spinel (Mg98) from Tanzania (top spectrum), and an Mg-spinel (Mg87) from Amity, NY (bottom spectrum).

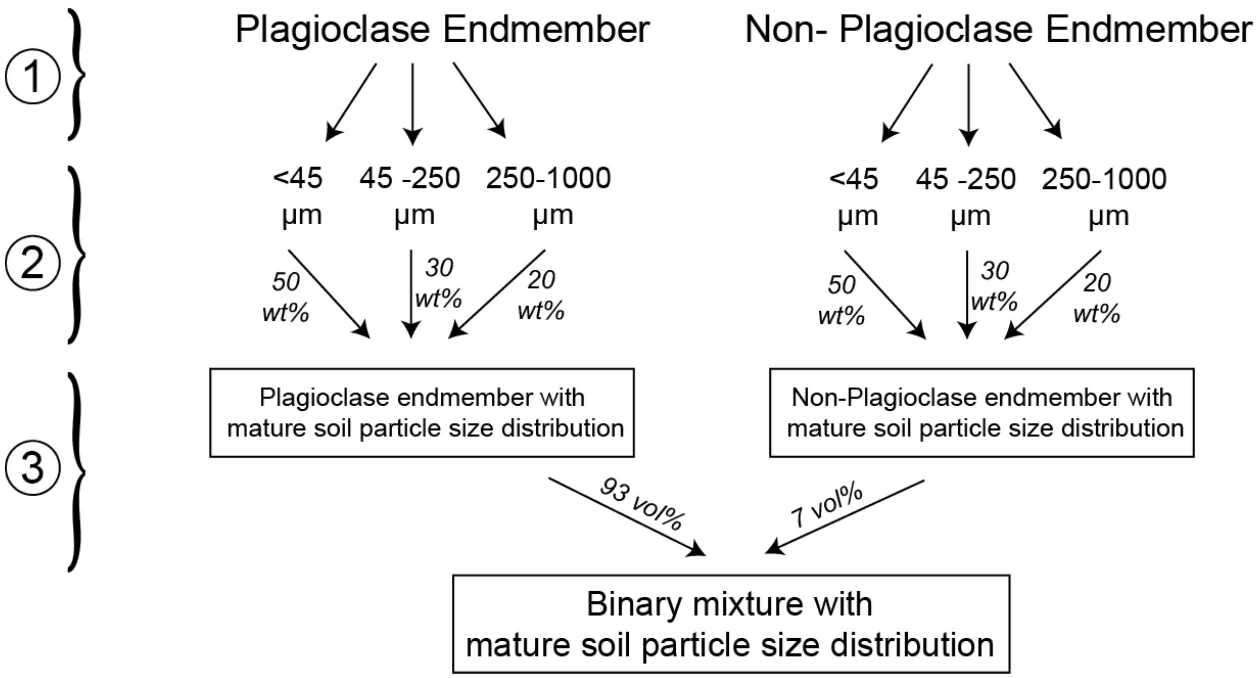

Figure 6. Sequence of mineral mixing procedures, using as an example the mature soil particle size distribution. In step 1, each of the mineral endmembers are divided into three broad particle size separates: <45 µm, 45-250 µm, and 250-1000 µm. In step 2, these three particle size fractions are combined in specific proportions by mass to create a distribution. In this case, the <45 µm, 45-250 µm, and 250-1000 µm splits go to represent 50%, 30%, and 20% by mass, respectively (for the immature distribution, they are combined as 20%, 30%, 50%, respectively). In step 3, binary mixtures of 93 vol% plagioclase and 7 vol% non-plagioclase endmembers, each containing a wide particle size distribution, are combined.

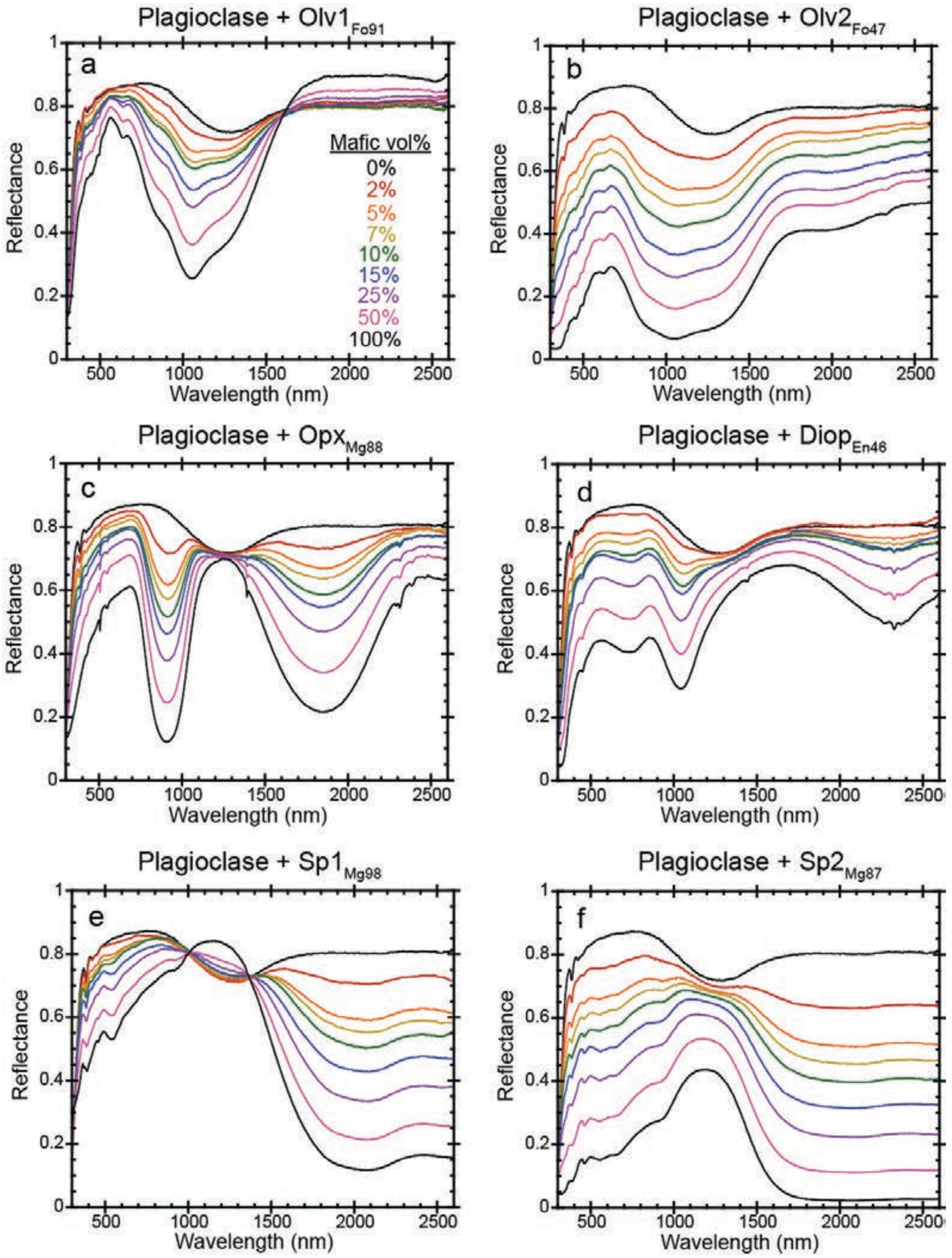

Figure 7. All six binary mixture series with particle sizes 45-75 µm produced for this study. (a) Plagioclase plus variable amounts of Olv1$_{Fo91}$. The legend and color scheme are the same in subsequent parts of the figure, (b) Plagioclase plus Olv1$_{Fo47}$, (c) plagioclase plus Opx$_{Mg88}$, (d) plagioclase plus Diop$_{En46}$, (e) plagioclase plus the Sp1$_{Mg98}$ endmember, (f) plagioclase plus the Mg-Spinel endmember.

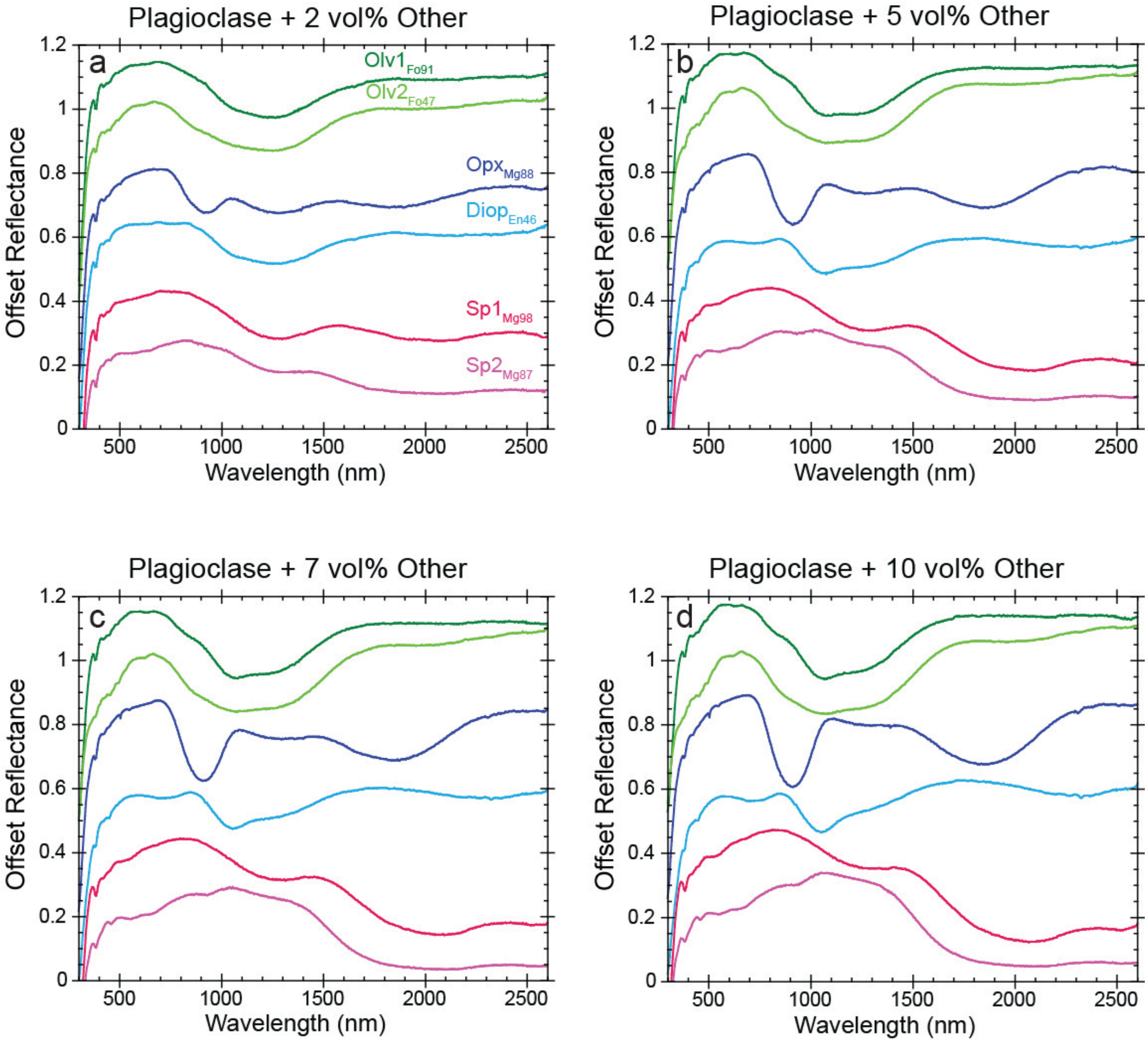

Figure 8. Mixture series (45-75 µm particles) displayed according to the volume percent of olivine, pyroxene, or spinel in each mixture. Only the mixtures that are strictly analogous to anorthosites, containing ≥90 vol% plagioclase, are shown (a) The six binary mixtures containing plagioclase plus 2 vol% non-plagioclase minerals. The spectra are labeled in part a only, but their order and color is maintained throughout all parts of the figure. (b) Mixtures containing plagioclase plus 5 vol% non-plagioclase minerals, (c) mixtures containing plagioclase plus 7 vol% non-plagioclase minerals, (d) plagioclase plus 10 vol% non-plagioclase minerals, (e) plagioclase plus 15 vol% non-plagioclase minerals, (f) plagioclase plus 25 vol% non-plagioclase minerals.

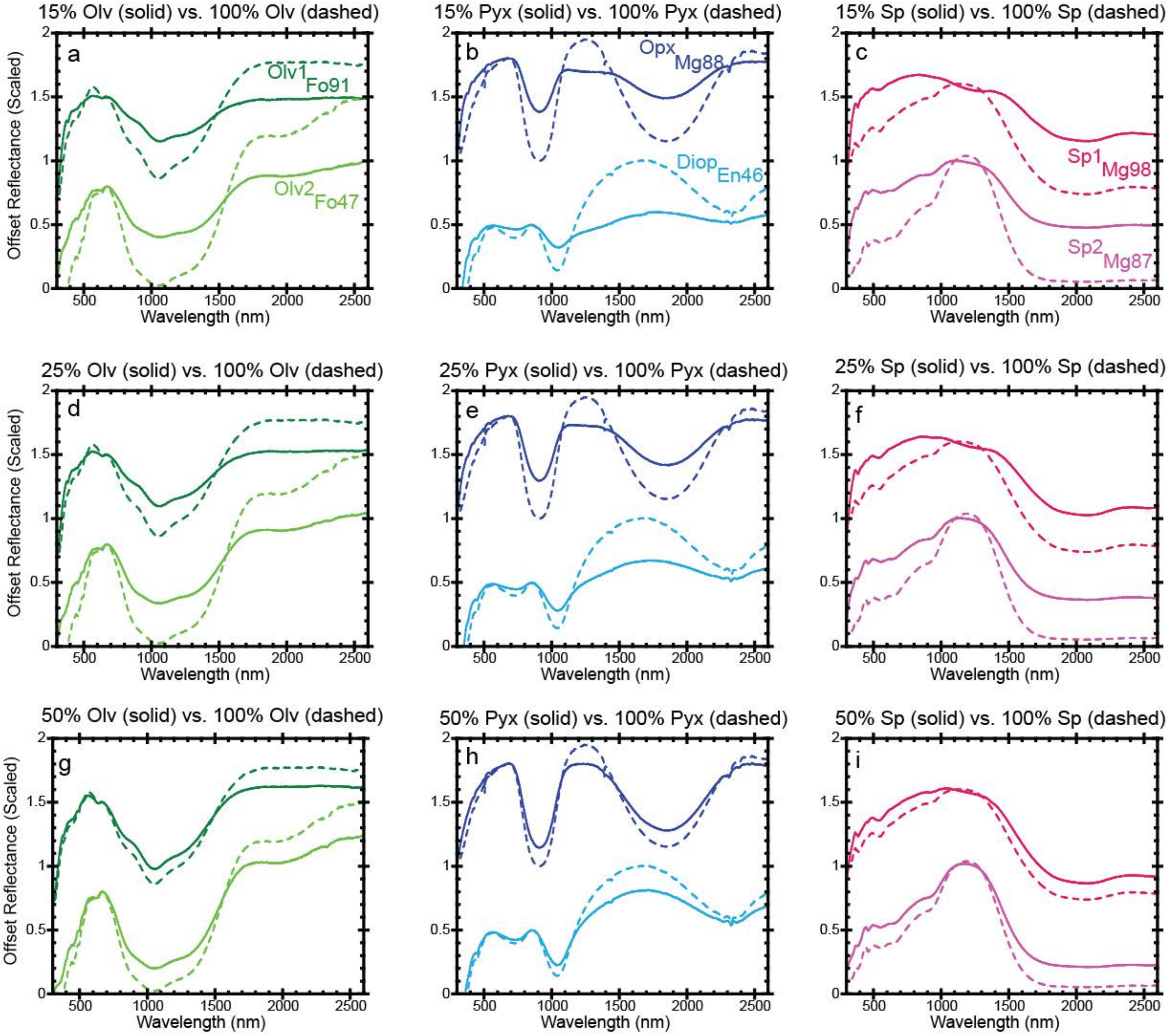

Figure 9. Laboratory prepared mixtures containing 15 (a-c), 25 (d-f), or 50 (g-i) vol% olivine, pyroxene, or spinel (45-75 µm particles). The corresponding mineral endmembers are plotted as dashed lines, the mixtures are plotted as solid lines. The endmember and mixture spectra have been scaled near the reflectance maximum below 1000 nm, and each pair of spectra was vertically offset for clarity. (a) 15 vol% olivine, (b) 15 vol% pyroxene, (c) 15 vol% spinel, (d) 25 vol% olivine, (e) 25 vol% pyroxene, (f) 25 vol% spinel, (g) 50 vol% olivine, (h) 50 vol% pyroxene, (i) 50 vol% spinel.

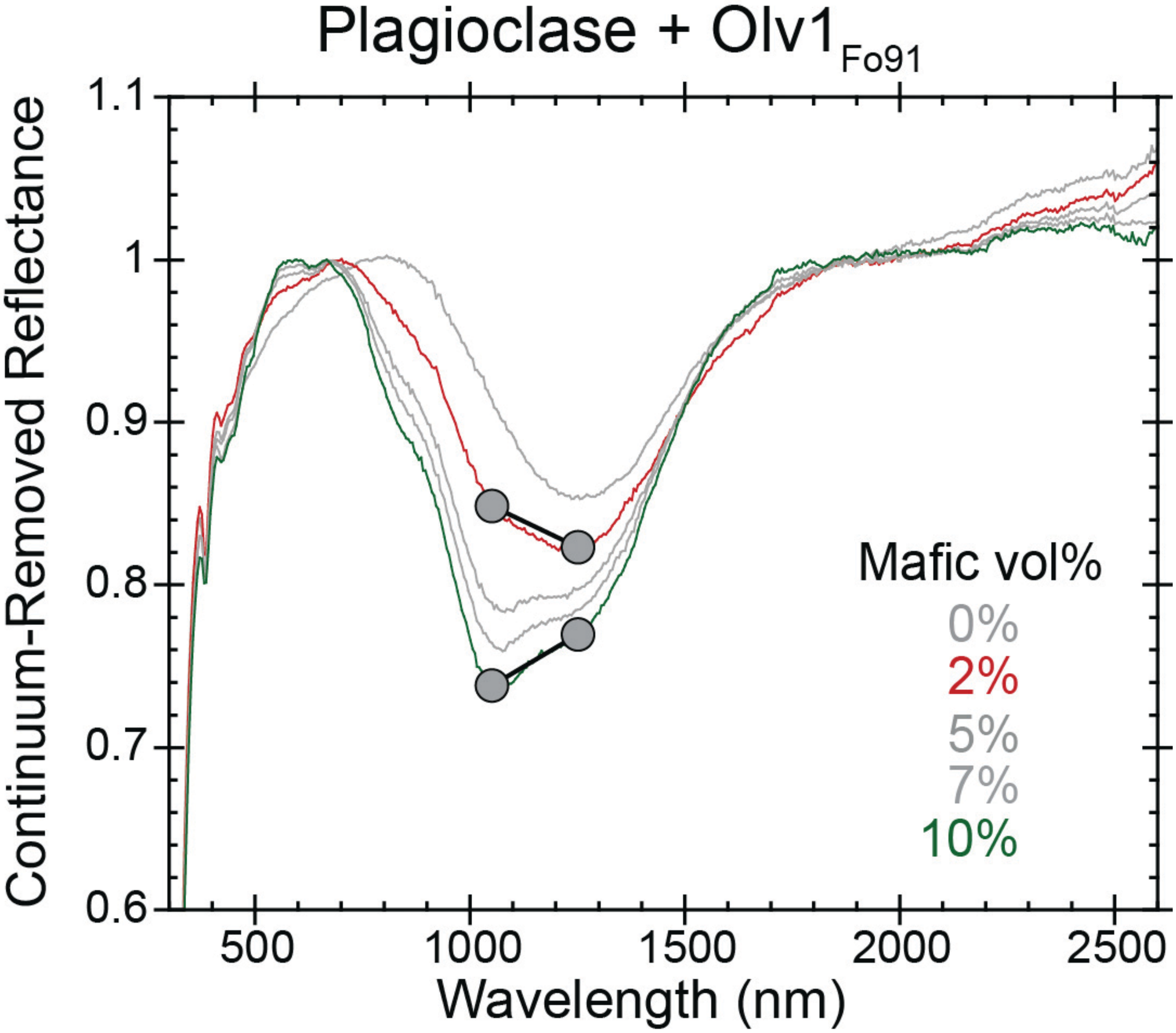

Figure 10. Schematic of the parameter for estimating relative band depths of the plagioclase and mafic components in a given spectrum, shown for two of the mixtures containing Olv1$_{Fo91}$. A negative slope for the 2 vol% olivine mixture corresponds to a relatively strong plagioclase component. A positive slope for the 10 vol% olivine mixture indicates a more dominant mafic component.

Always consult and cite the final, published document. See http://www.minsocam.org or GeoscienceWorld

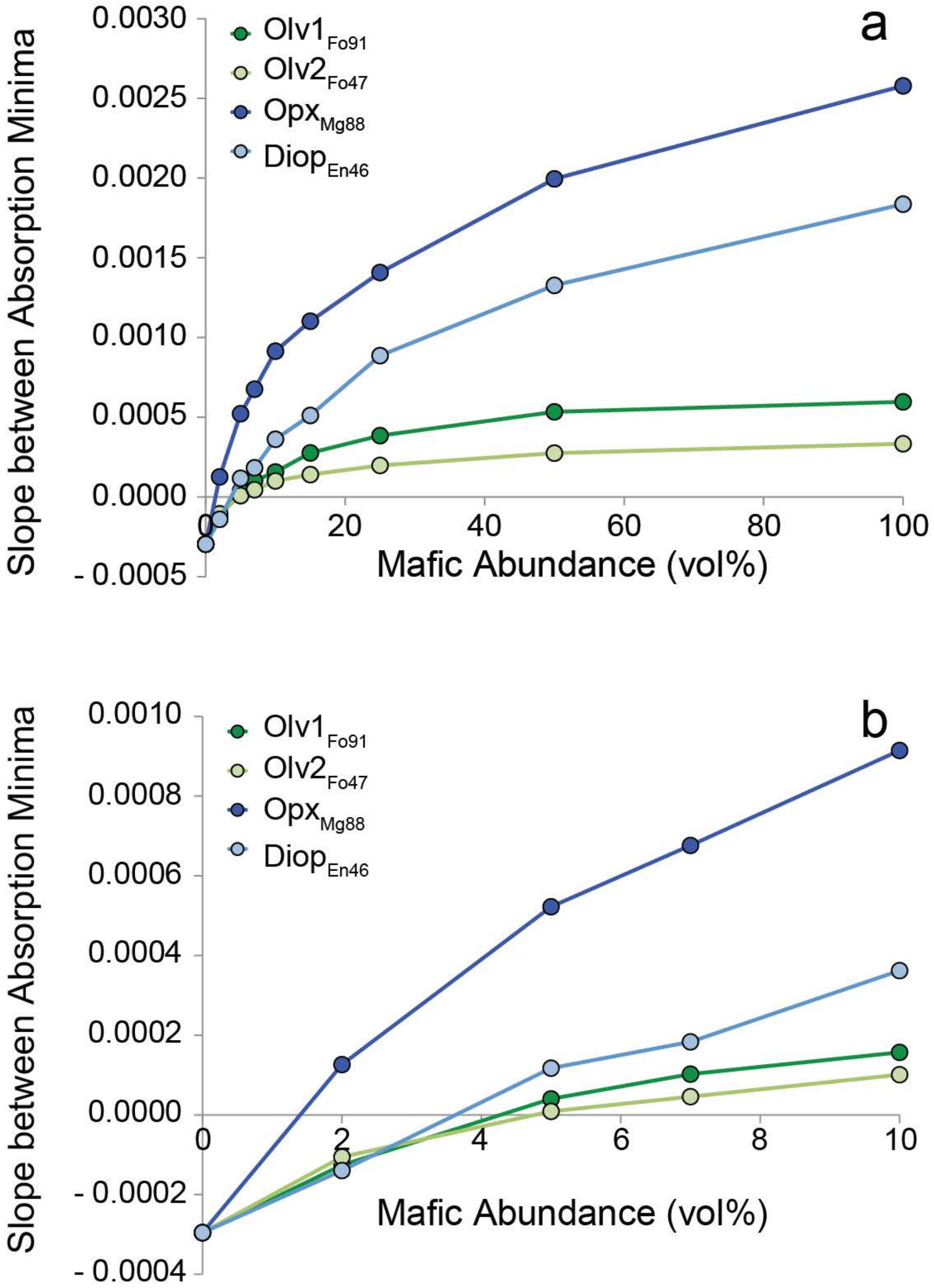

Figure 11. Slope parameter estimating relative plagioclase-mafic absorption depths. Higher slope values correspond to a relatively stronger mafic absorption. (a) Slope parameter values shown for all mixtures in the four mafic silicate series. (b) Slope parameter values shown for only the mixtures containing ≤10 vol% mafics.

Always consult and cite the final, published document. See http://www.minsocam.org or GeoscienceWorld

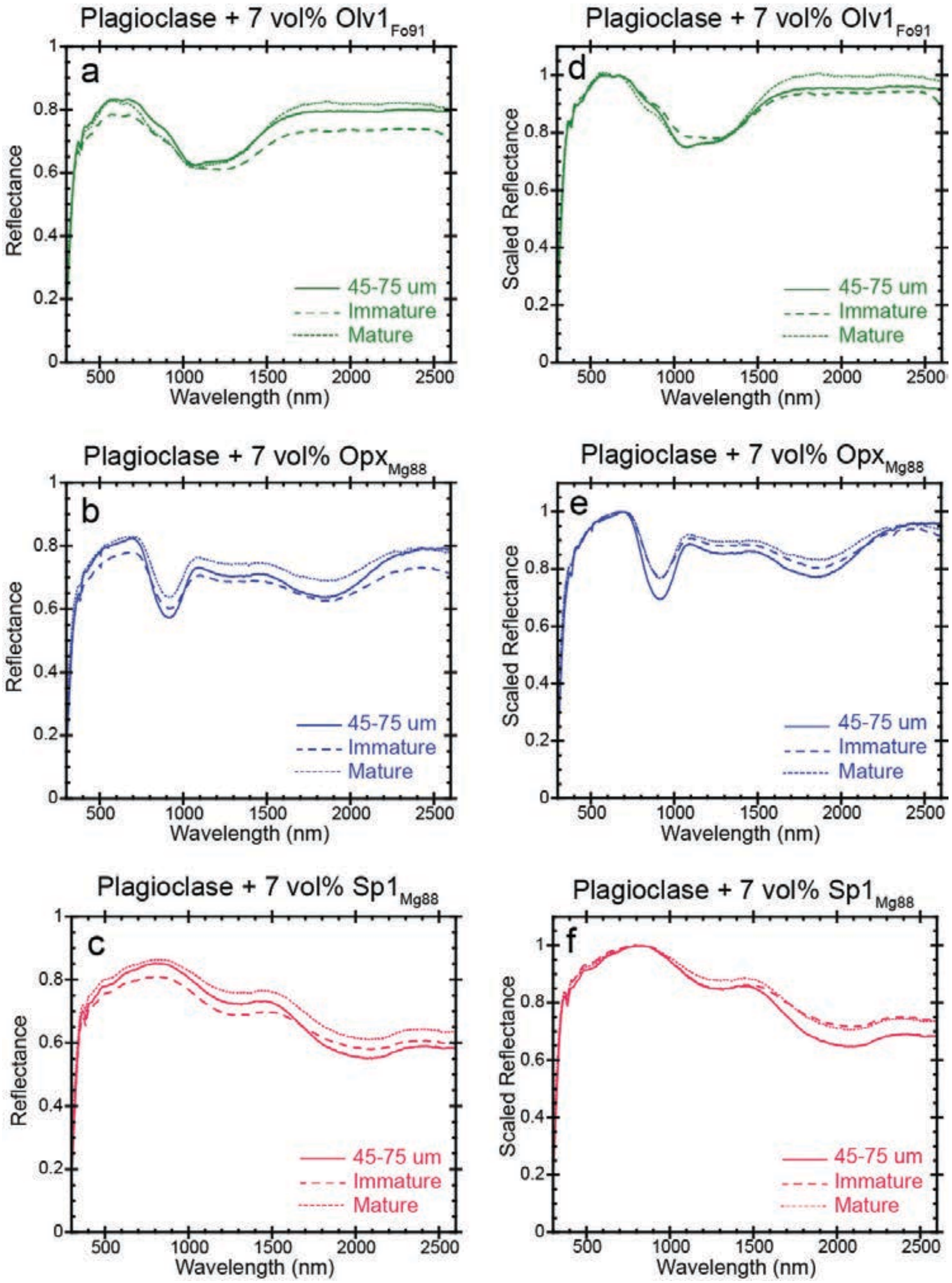

Figure 12. Two different soil size distributions compared with the constrained 45-75 μm size fraction for mixtures containing 7% olivine, pyroxene, or spinel. No continuum has been removed. (a) 7% Olv1$_{Fo91}$, (b) 7% Opx$_{Mg88}$, (c) 7% Sp1$_{Mg98}$, (d) 7% Olv1$_{Fo91}$, scaled to the reflectance maximum between 650 and 800 nm, (e) 7% Opx$_{Mg88}$, scaled as in (d), (f) 7 vol% Sp1$_{Mg98}$, scaled as in (d).

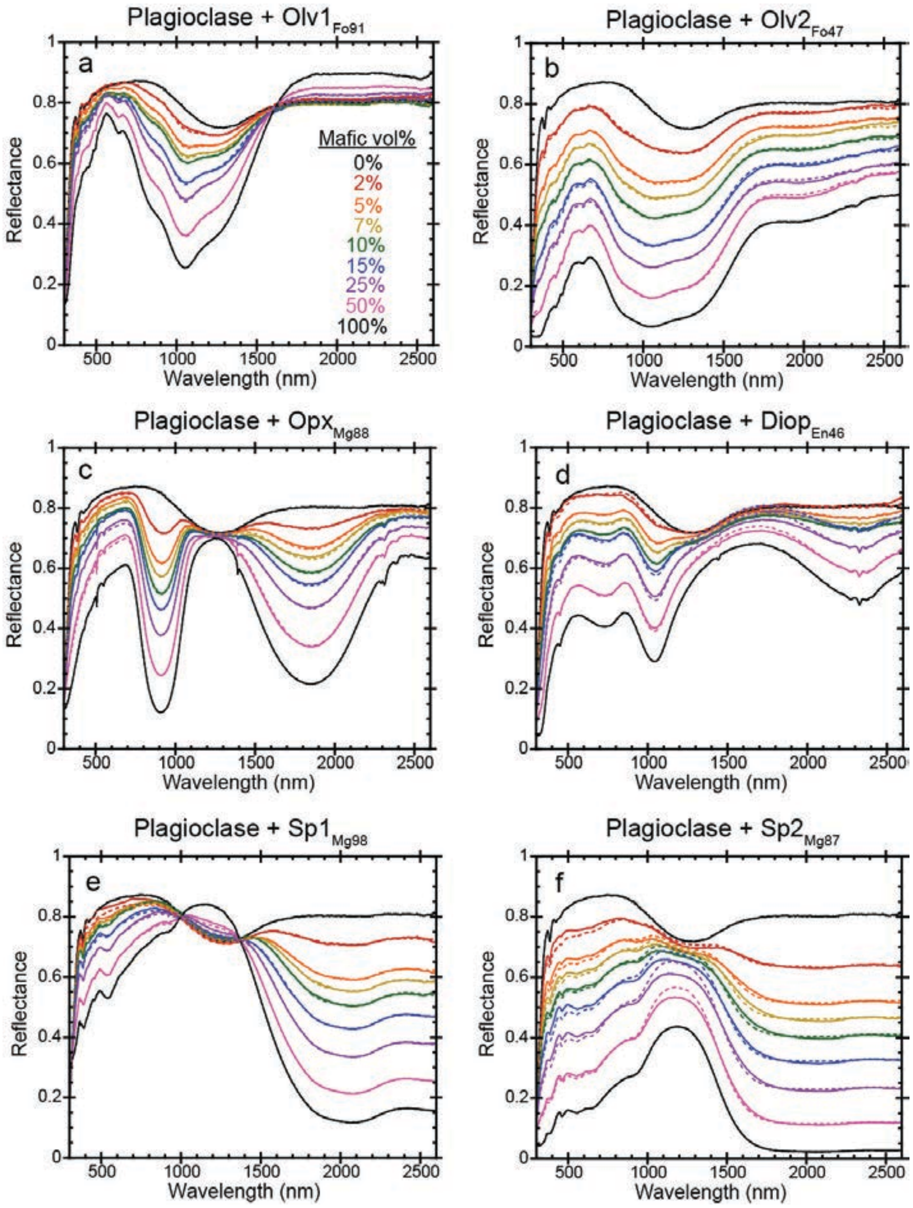

Figure 13. All six laboratory prepared mixture series (solid lines), the same as in Figure 7, plotted with the best fit modeled mixtures calculated using the inverse Hapke modeling approach (dotted lines).

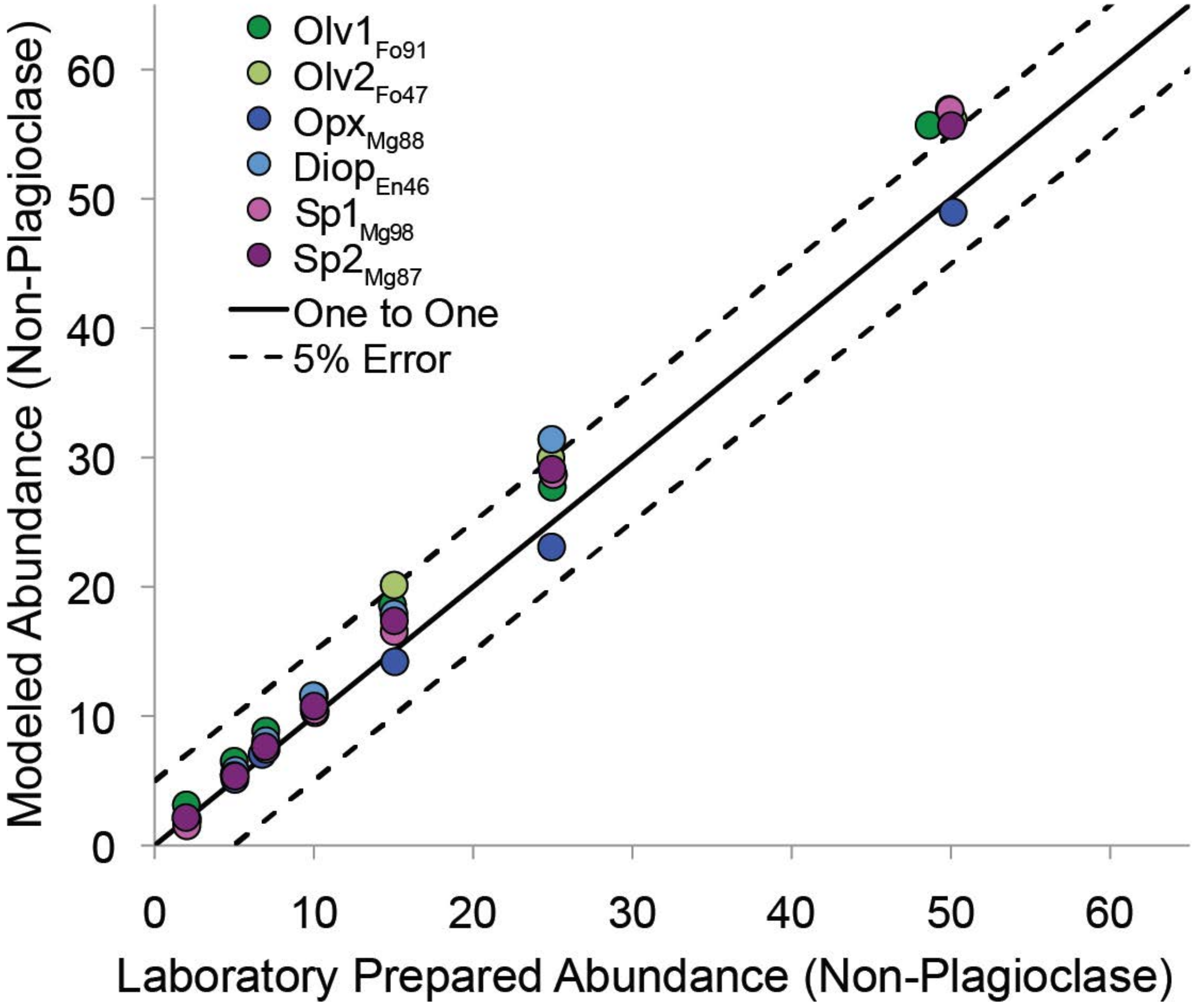

Figure 14. The non-plagioclase abundance (vol% solids) of the best-fit modeled spectrum plotted against the abundances prepared in the laboratory.

Always consult and cite the final, published document. See http://www.minsocam.org or GeoscienceWorld

This is a preprint, the final version is subject to change, of the American Mineralogist (MSA)
Cite as Authors (Year) Title. American Mineralogist, in press.
(DOI will not work until issue is live.) DOI: http://dx.doi.org/10.2138/am-2014-4785

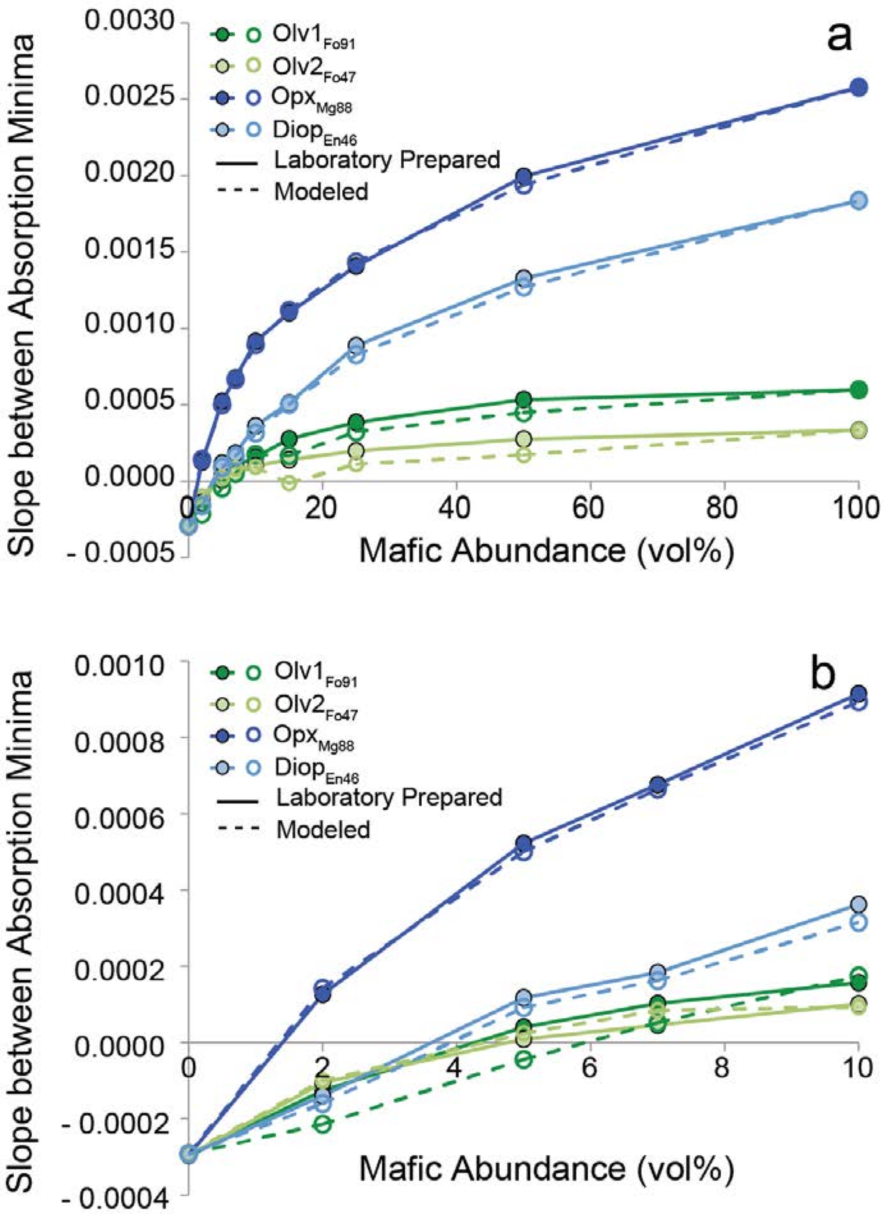

Figure 15 Proportion of mafic minerals in each best-fit modeled spectrum compared with the proportion of mafics in the corresponding laboratory prepared mixture. More positive slope values correspond to a higher mafic mineral abundance. A slope of zero corresponds to equal plagioclase and mafic absorption band depths, and negative values indicate that the plagioclase absorption is deeper than the mafic absorption in the continuum-removed spectrum. (a) Comparison of measured vs. modeled absorption depths for all mixtures. (b) Comparison of measured vs. modeled absorption depths for only the mixtures containing mafic abundances ≤10 vol%.

Always consult and cite the final, published document. See http://www.minsocam.org or GeoscienceWorld

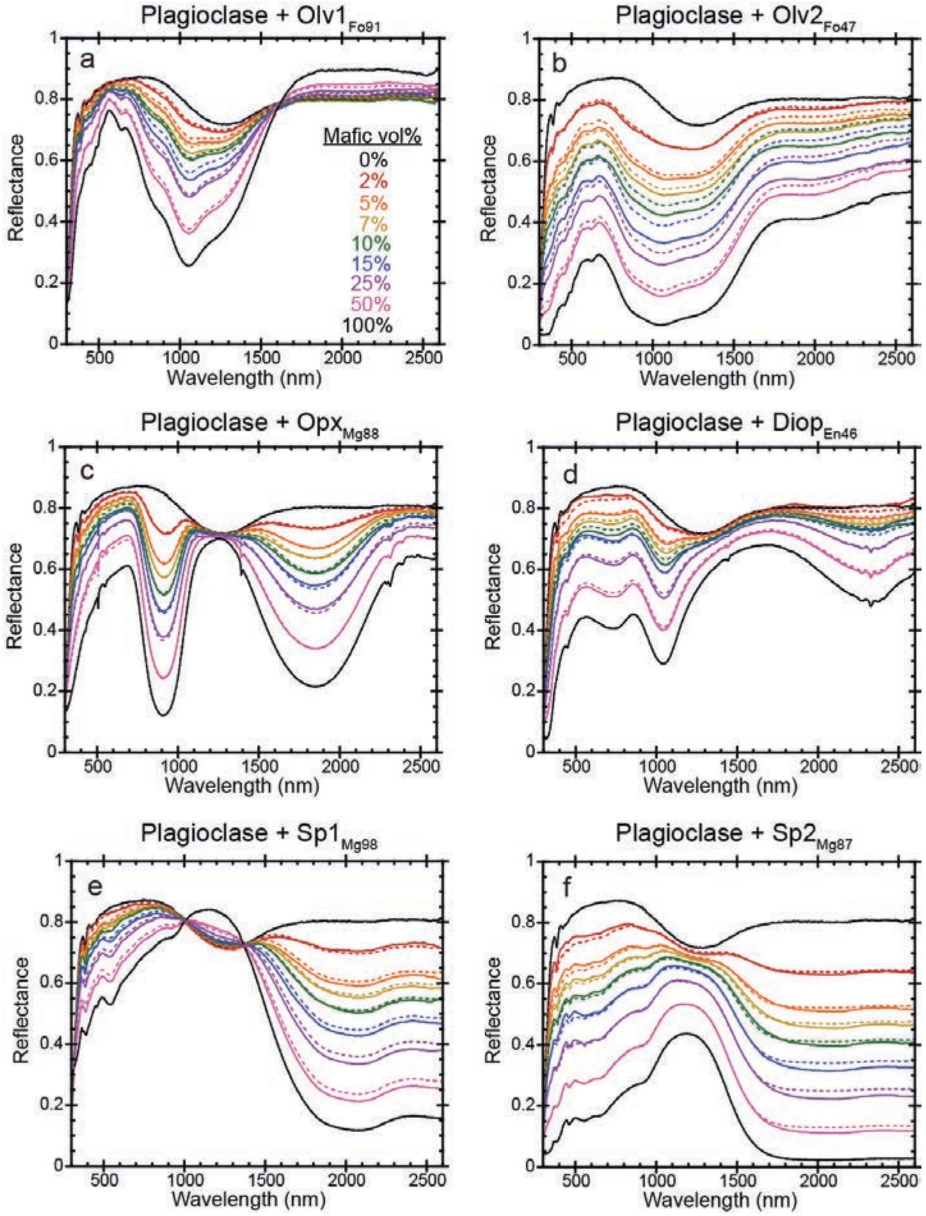

Figure 16. All six laboratory mixture series (solid lines), the same as in Figure 6, plotted with modeled mixtures calculated using the forward modeling approach (dotted lines).

Always consult and cite the final, published document. See http://www.minsocam.org or GeoscienceWorld

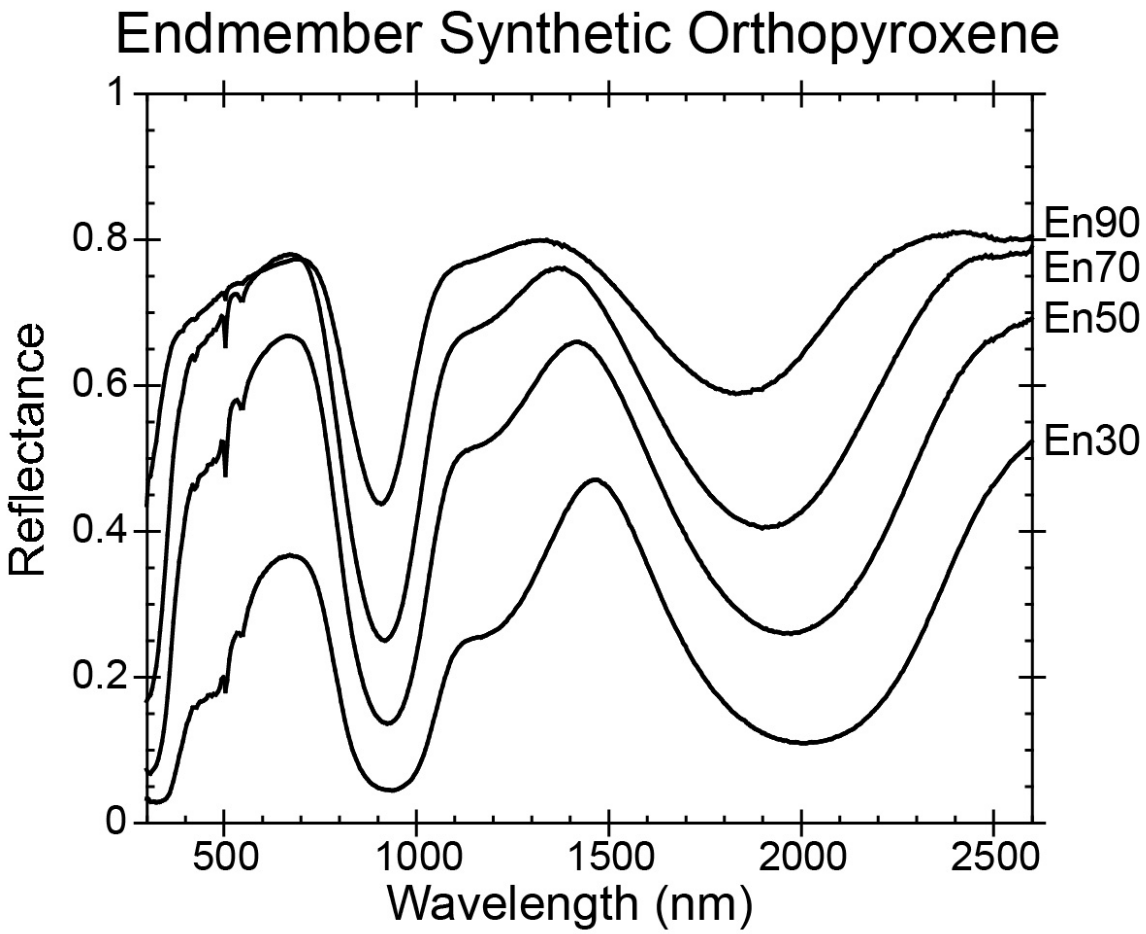

Figure 17. Endmember synthetic orthopyroxenes used in a forward model to characterize the effect of pyroxene composition on the spectra of plagioclase-dominated mixtures. These samples are from the suite studied by Klima et al. (2007), and were specifically chosen to span a wide range of En numbers. En90: RELAB ID: DL-CMP-065. En70: RELAB ID DL-CMP-026. En50: RELAB ID DL-CMP-004. En30: RELAB ID DL-CMP-023.

Always consult and cite the final, published document. See http://www.minsocam.org or GeoscienceWorld

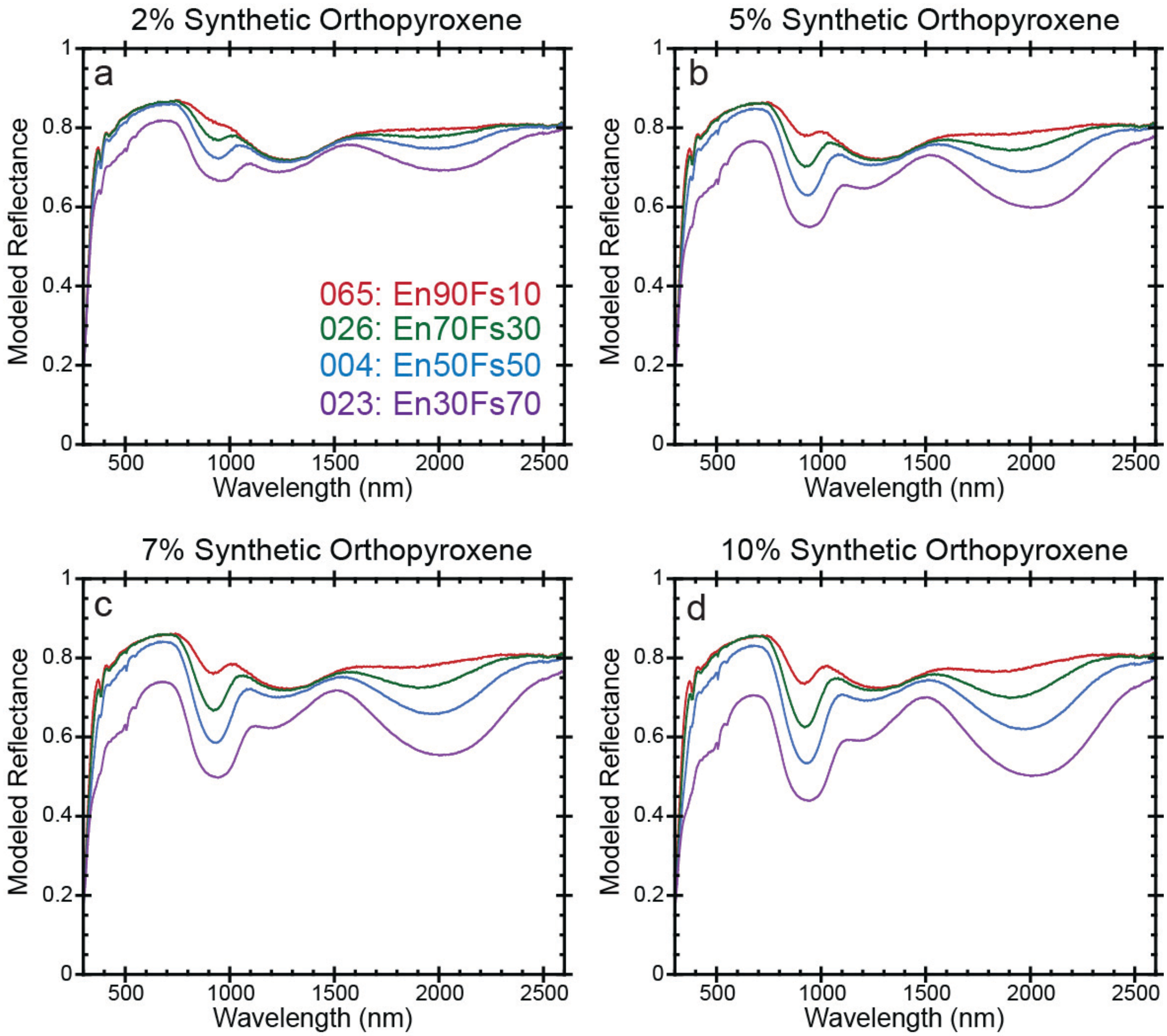

Figure 18. Model plagioclase – orthopyroxene mixtures produced using the Hapke forward model, with four synthetic orthopyroxene spectra as the mafic endmember (Klima et al. 2007). (a) 2 vol% orthopyroxene, (b) 5 vol% orthopyroxene, (c) 7 vol% orthopyroxene, (d) 10 vol% orthopyroxene.

APPENDIX: Residual Spectra

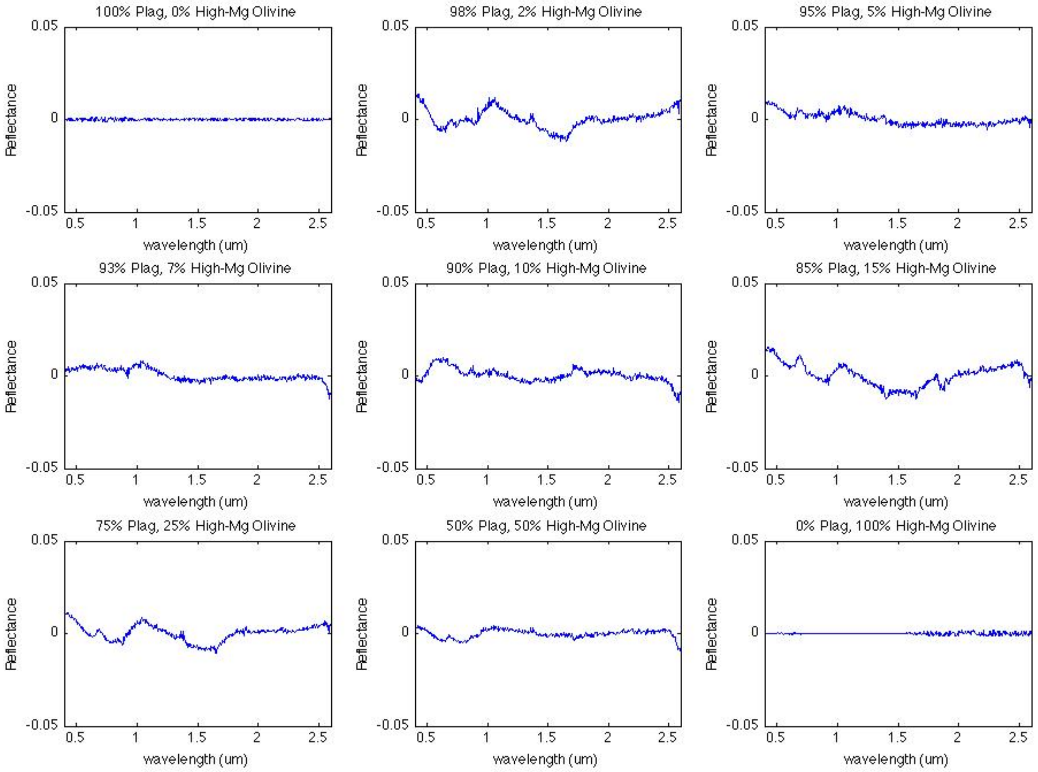

Figure A1. Residual Spectra (measured – best fit modeled spectra in reflectance) for the Plagioclase + Olv1$_{Fo91}$ series. The measured spectra were prepared in the laboratory with a particle size range of 45-75 μm. The modeled spectra were calculated using the inverse Hapke model with best fit proportions constrained to be positive and normalized to one.

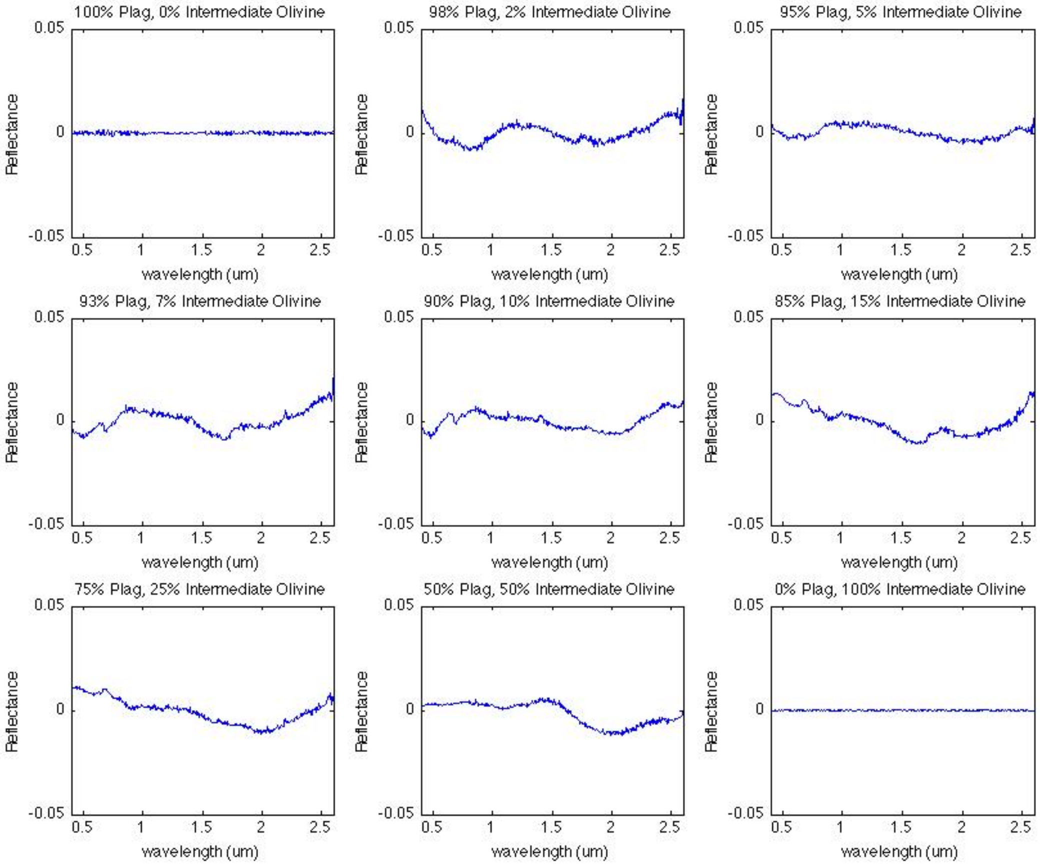

Figure A2. Residual Spectra (measured – best fit modeled spectra in reflectance) for the Plagioclase + Olv2$_{Fo47}$ series. The measured spectra were prepared in the laboratory with a particle size range of 45-75 µm. The modeled spectra were calculated using the inverse Hapke model with best fit proportions constrained to be positive and normalized to one.

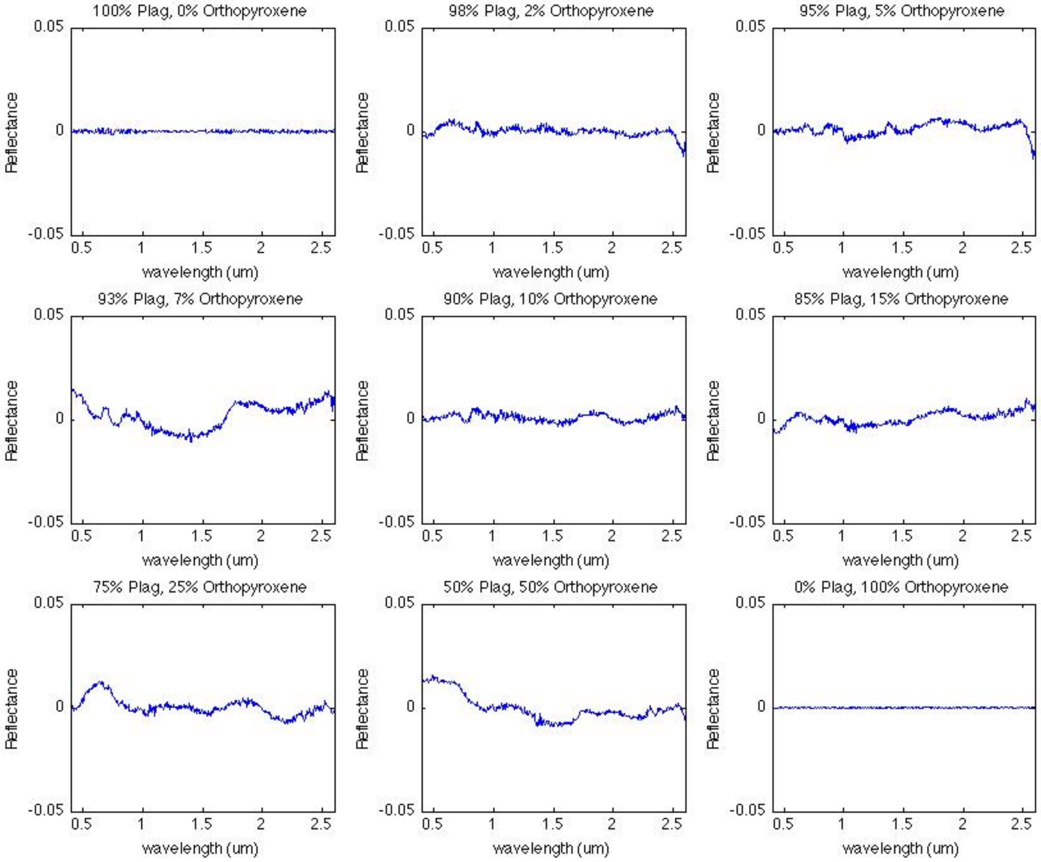

Figure A3. Residual Spectra (measured – best fit modeled spectra in reflectance) for the Plagioclase + Opx_{Mg88} series. The measured spectra were prepared in the laboratory with a particle size range of 45-75 µm. The modeled spectra were calculated using the inverse Hapke model with best fit proportions constrained to be positive and normalized to one.

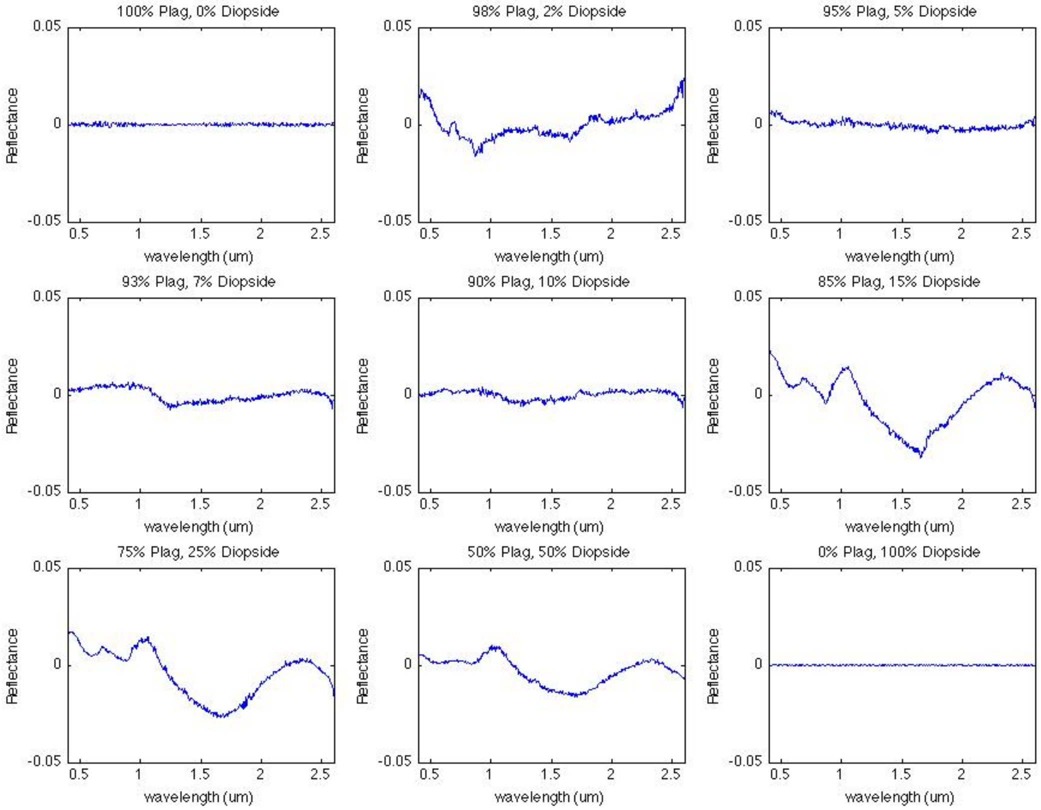

Figure A4. Residual Spectra (measured – best fit modeled spectra in reflectance) for the Plagioclase + $Diop_{En46}$ series. The measured spectra were prepared in the laboratory with a particle size range of 45-75 µm. The modeled spectra were calculated using the inverse Hapke model with best fit proportions constrained to be positive and normalized to one.

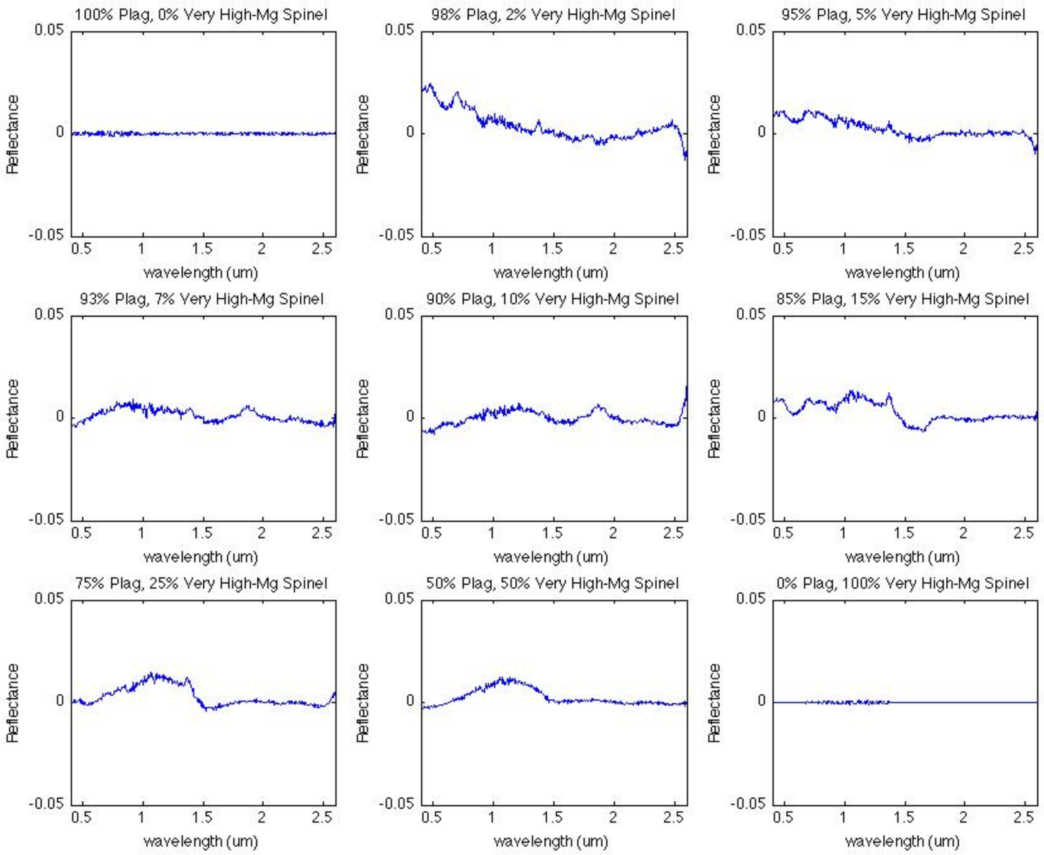

Figure A5. Residual Spectra (measured – best fit modeled spectra in reflectance) for the Plagioclase + Sp1$_{Mg98}$ series. The measured spectra were prepared in the laboratory with a particle size range of 45-75 µm. The modeled spectra were calculated using the inverse Hapke model with best fit proportions constrained to be positive and normalized to one.

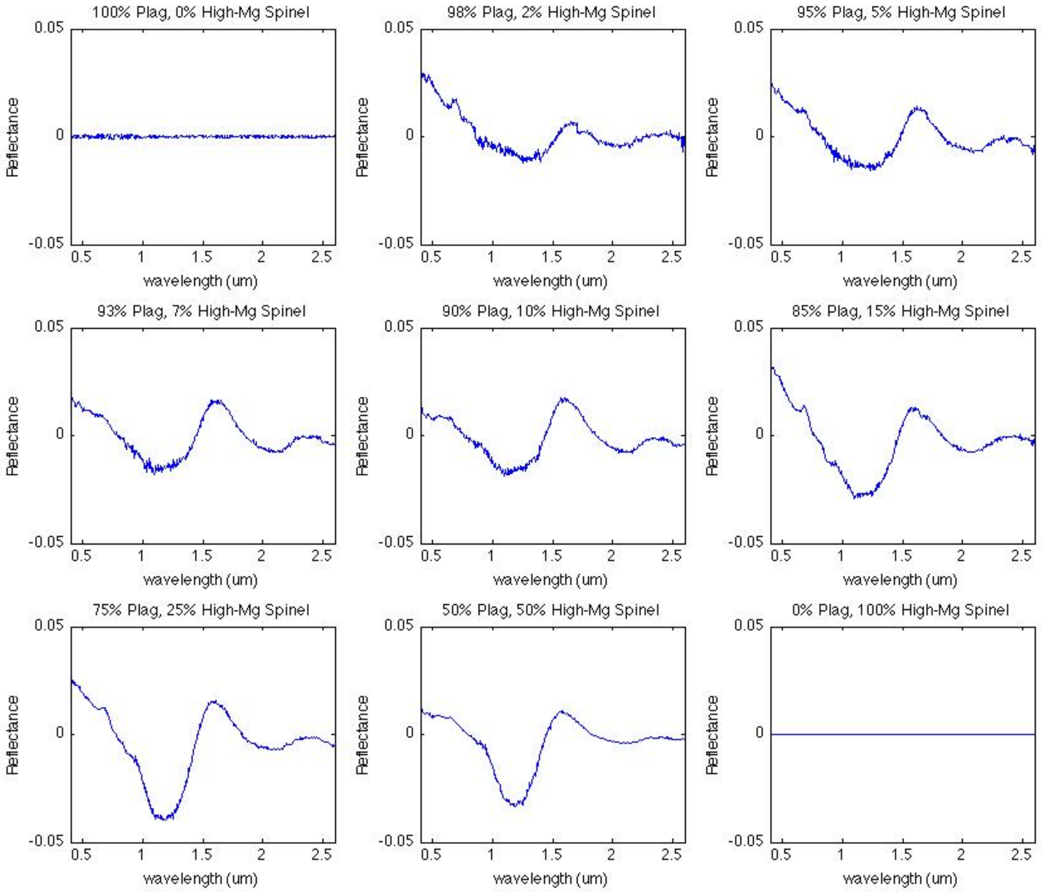

Figure A6. Residual Spectra (measured – best fit modeled spectra in reflectance) for the Plagioclase + $Sp2_{Mg87}$ series. The measured spectra were prepared in the laboratory with a particle size range of 45-75 µm. The modeled spectra were calculated using the inverse Hapke model with best fit proportions constrained to be positive and normalized to one.